Department of Physics and Astronomy
University of Heidelberg

Bachelor Thesis in Physics
submitted by

Viviane Charlotte Schmidt

born in Wiesbaden (Germany)

2018

Design of an ion beam extraction optics and analysis of the molecular composition of an ion beam in an electrostatic storage ring

This Bachelor Thesis has been carried out by Viviane Charlotte Schmidt at the
Max-Planck-Institut für Kernphysik in Heidelberg
under the supervision of
Prof. Dr. Klaus Blaum
and Dr. Sebastian George

Design einer Ionenstrahl-Extraktionsoptik und die Analyse des molekularen Aufbaus eines Ionenstrahls in einem elektrostatischen Speicherring:

Am kryogenen Speicherring (CSR) am Max-Planck-Institut für Kernphysik in Heidelberg eröffnen sich neue Forschungsmöglichkeiten in Form von kalten, molekularen Ionenstrahlen. Um die Auswahl an Ionenarten zu vergrößern, wird momentan eine 5 keV Strahlführungslinie gebaut, welche eine Vielzahl von Quellen mit der Injektionsstrahlführung des CSR verbinden soll. Eine anpassungsfähige Ionenoptikkonfiguration wurde während dieser Arbeit entwickelt. Diese kann sowohl zum Extrahieren von Strahlen mit hoher, als auch mit niedriger Emittanz verwendet werden, wodurch sie auf eine breite Auswahl an Ionenquellen anwendbar ist. Um das effiziente Experimentieren an Strahlen mit Intensitäten unterhalb der Nachweisgrenze der Diagnostiksysteme des CSR zu ermöglichen, werden hier zwei alternative Methoden zur Bestimmung der Umlauffrequenz der Ionen vorgestellt. Auf Grund der unzureichenden Massenauflösung der Umlenkmagneten besteht die Notwenigkeit, die Masse der Teilchen zusätzlich im Ring zu bestimmen. Hierfür konnte sowohl die Beobachtung eines Ionenpaketes im Ring, als auch die verzögerte Eletronenablöse bei negativ geladenen Ionen mittels Laserbeschuss verwendet werden. Mit Hilfe der Massenspektren der Quellenprodukte und der vom Ionenstrahl im CSR erzeugten Fragmente konnte außerdem die molekulare Zusammensetzung der Strahls analysiert werden. Zusätzlich stellten sich die beiden Methoden als effektives Mittel zur Bestimmung von nicht-isobaren beziehungsweise isobaren Kontaminationen heraus.

Design of an ion beam extraction optics and analysis of the molecular composition of an ion beam in an electrostatic storage ring:

New research opportunities are available in form of cold molecular beams stored in the electrostatic Cryogenic Storage Ring (CSR) at the Max-Planck-Institut für Kernphysik in Heidelberg. To expand the range of available ion species, a 5 keV ion transfer beamline is currently under construction to connect a variety of sources to the injection beamline of the CSR. Versatile ion beam extraction optics were developed during this thesis, which can be applied to sources producing low and high emittance beams alike. To efficiently experiment even with beams of intensities below the detection threshold of the diagnostic systems of the CSR, two alternative procedures to determine the revolution frequency and consequentially the mass of the stored ions are presented. Due to the insufficient mass resolution of the bending magnets in the injection beamline, a method of mass verification is necessary for heavy particles. The observation of an ion bunch in the ring and delayed electron emission after laser excitation are successfully applied for this purpose. Furthermore, an analysis of the molecular composition of the beam is performed using mass spectra of the source output and the charged fragments of the beam. In addition, they also proof effective to identify non-isobaric and isobaric contaminations, respectively.

Contents

1 Introduction

The electrostatic Cryogenic Storage Ring (CSR) [1] at the Max-Planck-Institut für Kernphysik in Heidelberg offers a unique opportunity to study atoms and molecules in an environment alike the interstellar medium. Ions can cool down radiatively to their rovibrational ground state due to the cryogenic conditions in the ring. A wide range of diagnostic and experimental equipment enable a variety of experimental techniques.

To study even rarely produced ions, sophisticated ion sources have to be implemented on the high voltage platforms of the CSR, which produce a variety of different molecules and clusters, as e.g. CH^+, Ag^-, etc. A 5 keV transfer beamline is currently being installed on one of the platforms, enabling the combination of various types of ion sources and preparation traps in parallel. A versatile ion beam extraction configuration for this setup was developed during this thesis.

Due to the low beam current of exotic ion species, the standard pick-up system in the CSR (e.g. Schottky pick-up) are unable to detect the stored ion beam, arising the need for a different method of mass determination in the mass independent electrostatic storage ring. Furthermore, as the mass of the molecules and its complexity increases, so does the number of possibilities for isobaric contaminations. Thus, a fragment scan is demonstrated to be an efficient tool to understand the molecular composition of the stored beam.

In chapter 2 of this thesis the CSR, its storage and detection principle, as well as the ion sources will be introduced. The simulation results of an ion beam extraction system are described in chapter 3, followed by the presentation of an analysis method of the molecular composition of an ion beam stored in the CSR in chapter 4. Finally, a conclusion and an outlook are given.

2 The Cryogenic Storage Ring (CSR)

This chapter briefly discusses the most common concepts of storing charged particles (section 2.1), before introducing the electrostatic Cryogenic Storage Ring (CSR) and its ion sources at the Max-Planck-Institut für Kernphysik in Heidelberg (section 2.2).

2.1 Storing Charged Particles

In order to perform experiments with charged particles, three dimensional confinement under well-controlled conditions is crucial. The Lorentz force

$$\vec{F}_L = q(\vec{E} + \vec{v} \times \vec{B}), \tag{2.1}$$

generated by both magnetic $\vec{B}$ and electric fields $\vec{E}$, is suited to manipulate the motion of particles of charge q and velocity $\vec{v}$ accordingly. Over the past decades, various configurations of dynamical and static electric fields, as well as static magnetic fields were used for this purpose.

Ion traps and storage rings are two classes of storage devices for charged particles. The two most prominent representatives of the former are Paul [2] and Penning traps [3]. The Paul trap uses a static and an oscillating electric field to generate a trapping potential. It is often used as a mass filter or an ion buncher in two dimensions. The Penning trap, on the other hand, employs both electric and magnetic fields to confine ions. Due to the well-known trajectory of the charged particles inside the trap, it can be used for high-precision mass spectrometry experiments [4].

Magnetic storage rings were primarily developed for high-energy particle physics [5], before being used in nuclear, atomic and molecular physics [6]. In order to increase its versatility in the latter fields of physics electrostatic storage rings were developed [7].

2.1.1 Storage Rings

In storage rings, eq. (2.1) acts as a centripetal force

$$F_C = \frac{mv^2}{r} \tag{2.2}$$

and confines the ions of mass m on a closed orbit with radius r.

The first such devices were magnetic storage rings ($E = 0$). With a mass dependent bending radius

$$r = \frac{\sqrt{2E_{kin}m}}{qB},$$ (2.3)

for non-relativistic particles of energy E_{kin} and

$$r = \frac{vm}{qB}$$ (2.4)

for relativistic ions, they are ideally suited to study fast, light particles. Due to the high energy of the stored ions, the cross-section for beam - residual gas collisions are sufficiently low to achieve storage times of hours at relatively high background pressure of about $\sim 10^{-9}$ mbar [8].

To study heavier, low energy ion beams, electrostatic storing rings were developed. In the absence of the magnetic field ($B = 0$), the bending radius

$$r = \frac{2E_{kin}}{qE}$$ (2.5)

is now directly proportional to the kinetic energy and mass independent. The device itself is therefore not mass-selective, i.e. storing all species within the kinetic energy acceptance of the ring settings. A procedure to analyse the mass composition of an ion beam stored in an electrostatic storage ring is discussed in chapter 4.

2.1.2 Manipulation of Stored Ions

Internal states and the motion of stored particles can be manipulated. The eigenmotions can be altered by excitation with a resonant rf signal. This can be employed to remove unwanted ions in a storage devices, for instance, as is often done in Penning traps [9]. To study internal states, laser excitation can be applied to observe ionization, fragmentation or electron detachment processes.

It is also possible to cool the internal states of an ion or the phase space of the ion motion. Using Coulomb interaction of the stored ions with an electron beam [10] or momentum transfer with buffer gas [11], the volume of a particle beam in the phase space can be reduced. It is also possible to cool internal states of single ions via laser excitation [12] or thermal radiation [13]. In the CSR, stored ions can reach ground state excitation levels using radiative cooling within minutes [14].

2.2 Experimental Set-Up

The CSR is the electrostatic storage ring device at the Max-Planck-Institut für Kernphysik in Heidelberg [1]. It can be cooled to temperatures below $10\,\mathrm{K}$ by a closed-cycle helium refrigeration system achieving pressures equivalent to $10^{-12}\,\mathrm{mbar}$ at room temperature [15] and is therefore ideally suited to perform experiments on cold ion beams in a quasi background-free environment. The nearly quadratic device has a circumference of $35.12\,\mathrm{m}$, with ion optical elements in the corners 1-4 and experimental set-ups and beam diagnostics in the field free straight sections (A)-(D), as shown in figure 2.1.

The ion beams are produced on high-voltage platforms and guided to the ring, which can store particles with a kinetic energy up to $300\,\mathrm{keV}$ per charge unit. In section (A), the interaction between the ions and neutral particles can be studied [16]. Section (B) hosts an electron cooler used for phase space cooling of the stored beam and serving as an electron target for recombination experiments between positively charged particles and electrons [17]. This region also includes a laser interaction zone, where the ions can be probed by continuous wave (CW) or pulsed laser light.
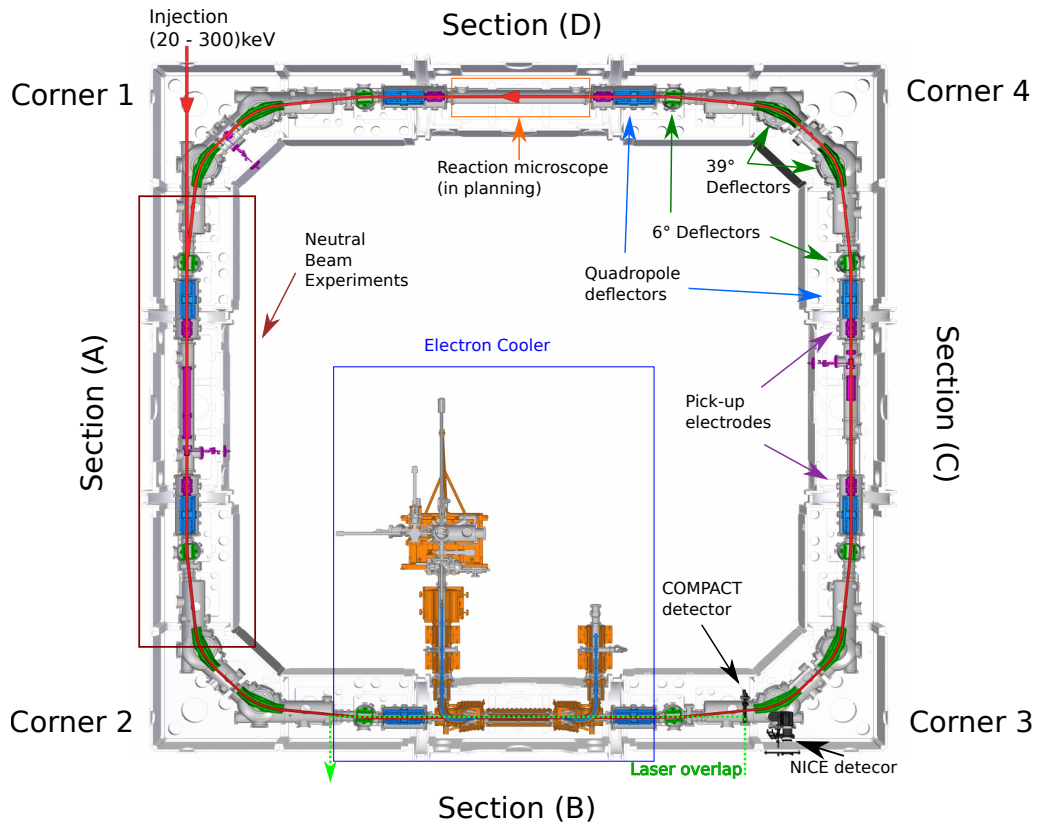

Figure 2.1: Schematics of the CSR, for details see text.

Section (C) is reserved for beam diagnostics [17]. A reaction microscope will be placed in section (D). In the following subsections, the experimental equipment relevant for this thesis will be discussed in detail.

2.2.1 Ion Sources

Three different kinds of sources are currently operated at the high voltage platforms. Penning sources [18] and an ECR source [19], which were not used for measurements in this thesis and therefore not discussed in the following, and sputter sources. In the near future, a laser evaporation source (LVAP) will be installed as well. Within this thesis, the simulation studies for the extraction optics of the LVAP source were performed and are discussed in chapter 3.

The Middleton sputter source (MISS) [20] produces negative ions by accelerating caesium cations towards a solid target containing the desired particle species. The harsh sputtering process creates a wide range of positive, negative and neutral species, whereas only negative ions are extracted from the source by electrostatic potentials. It is also possible to create molecules consisting of different atomic species, for example C_4O^-, which can be produced employing a carbon target in a dilute oxygen atmosphere. To influence the production cross section of a certain cluster or molecule, various source parameters can be optimised. The gas pressure regulates the available amount of oxygen, while the temperature of the caesium oven defines the quantity of Cs^- in the source and therefore regulates the output current. Since a selection of a specific ion species is not possible within the source, a mass selection by bending magnets behind the extraction is often used to remove undesired species. Due to their harsh creation, the ions extracted from the source are rovibrationally excited covering a wide range of states.

In contrast to the MISS, the LVAP source is designed to create ions and molecules in low rovibrational states [21]. A pulsed laser is focused on a metal target and evaporates atoms, clusters and electrons, which are then flushed downstream through an expansion channel by a high-pressure carrier gas pulse (e.g. helium). There, the ions cool by supersonic expansion, exchanging energy with the buffer gas, leading to clusterization of larger species. While charged particles are extracted by an appropriate electrostatic potential, neutral particles are being pumped away. To achieve reasonable pressure behind the source, it is important to extract the ions, while minimizing the buffer gas flow out of the source. Differential pumping [22] can be applied, which allows for high pressure differences on short distances by using narrow orifices between various regions. A soft extraction can be used to prevent rovibrational excitation by rest gas collisions. A possible setup is discussed in chapter 3.

2.2.2 Ion Beam Diagnostics

To monitor the stored beam, three different pick-up electrode systems are used in the CSR (see figure 2.1). While three sets of position pick-ups are placed at the entrance and exit of the straight section (A), (C) and (D), two other types of pick-ups are employed in section (C) to determine the current and the Schottky noise [23], from which the multiples of the revolution time can be calculated using a Fourier transformation.

For destructive measurements, two multi-channel plate (MCP) detector systems are currently employed at the CSR, which will be briefly explained here.

  i) The COld Movable PArticle CounTer (COMPACT) detector (see figure 2.2 (a)) was developed to count single neutrals or charged fragments at various positions created in the field free straight section (B) in front of the detector [24]. The incoming particles hit a converter cathode and create secondary electrons, which are then accelerated towards an MCP detector. Neutrals and fragments are not stored at the closed orbit of the parent beam (see section 4.3). The detector, located behind the 6° deflector (see figure 2.1), can therefore be used to acquire a $\frac{m}{q}$ -spectrum of reaction products.

 ii) The Neutral particle Imaging in Cold Environment (NICE) detector (see figure 2.2 (b)) is placed in the neutral port of the 39° deflector in corner 3 (see figure 2.1). It consists of an MCP detector with a phosphor screen anode. The detector is designed for position imaging and high time resolution. The electrons from the MCP hit the phosphor screen, creating a light spot, which is then captured by a high-speed camera [25].
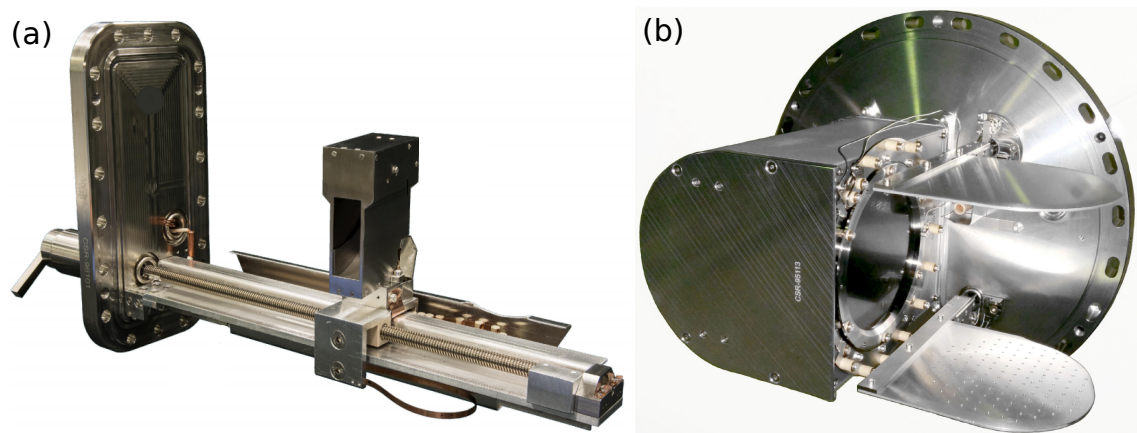

Figure 2.2: Images of the detectors used in the CSR: COMPACT detector [26] (a) and NICE detector [25] (b)

2.2.3 Laser setup

To excite the stored ions, laser beams can be overlapped with the ion beam in section (B) (see figure 2.1), either in a crossed-beam configuration or with a grazing angle. Figure 2.3 shows the laser path inside the CSR. The beam is guided in and out of the ring through view ports. The angle between laser and ion beam is $1.073°$ over a $1.67\,$m interaction region.

Within this thesis studies, a pulsed OPO laser was used to excite a subset of the beam. Thus, the excited ions are in a bunch of a few microsecond time spread (see section 4.2.2). Continuous wave (cw) laser beams are also employed for ion beam depletion or to create a continuous background signal for normalization.

2.3 Experimental Procedure

The aims of the experiments were to study laser-induced electron detachment and fragmentation processes in C_4O^-, as well as understanding its radiative cooling behaviour. A MISS source was optimised for C_4O^- production (see section 2.2.1). A mass selection was performed by dipole magnets in order to isolate the desired molecule, and the ion specie was afterwards verified in the storage ring. The proce-
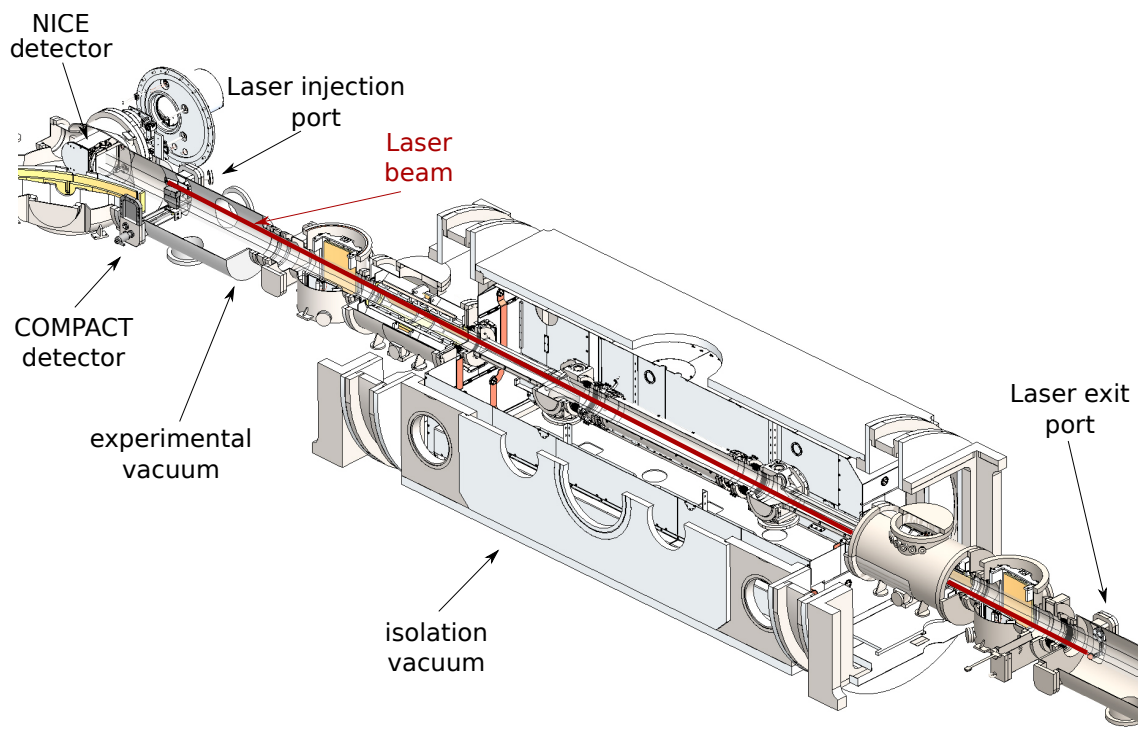

Figure 2.3: Laser setup inside CSR, for details see text.

dure for mass determination will be presented in chapter 4.

An OPO laser system, tunable from 410 nm to 2600 nm, was then used to excite a small fraction of the stored particles. Reaction products were recorded in dependence of laser energy and storage time by COMPACT and NICE (see section 2.2.2). Coincidence measurement of neutrals and fragments could be recorded using both detectors simultaneously.

The measurements described below were inspired by previous experiments on Co_4^- clusters conducted at the Cryogenic Trap for Fast ion beams (CTF) [27] MPIK [28]. There, delayed electron emission was used to study the internal energy distribution of the ions. To analyse the effect of cryogenic conditions on the ion's internal energy, a Co_4^- beam was produced in a MISS and within this thesis stored in the CSR, leading to the first measurements of the delayed electron emission in the in this device.

3 Simulation studies of an ion beam extraction system

This chapter discusses the ion optical simulation studies for an extraction system connecting a variety of ion source types, such as the new LVAP source (see section 2.2.1), with the 5 keV transfer beamline positioned on the CSR high-voltage platform. For this purpose, the software package SIMION was employed. It solves the Laplace equation to calculate the electrostatic fields before using the fourth-order Runge–Kutta method to obtain the ions' trajectory [29]. After an overview about standard extraction configurations (section 3.1), a new setup is introduced and the simulation studies performed to optimize the extraction of the ions are presented (section 3.2).

3.1 State-of-the-art extraction systems

The best known extraction configuration for a charged beam is probably the Pierce geometry, invented by J.R. Pierce in 1940 for rectilinear electron beams [30]. Neglecting any magnetic effect caused by the electron current, and thermal velocities, Pierce was able to derive a condition for the electric field ϕ at a given position x

$$\phi(x) = Ax^{\frac{4}{3}}, \tag{3.1}$$

with $A = 5.69 \times 10^3 j^{\frac{2}{3}}$ and j the field current density, which is satisfied by a zero potential surface with an 67.5° angle to the beam edge. With such a configuration, the equipotential lines are nearly symmetric around the beam axis. This setup was later used for the extraction of ion beams from sources as well, with only minor adaptations. To minimize the divergence and diameter of the extracted beam, configurations of multiple electrodes were implemented [31]. Programs such as SIMION were employed to optimize the extraction system [32].

3.2 Experimental Setup

The aim is developing a general extraction system for molecular ion beams of low and high emittance alike, which can for example be produced by LVAP sources or MISS (section 2.2.1), respectively. The ions are accelerated to 5 keV, matching

the kinetic energy of the transfer system of the CSR high voltage platform. The demands on the configuration are discussed in the following section.

3.2.1 Design criteria

Future projects at CSR require storing beams of complex molecules and clusters, for example $(SF_6^-)_N$, produced in LVAP sources. However, the large structure increases the risk of fragmentation or internal heating when colliding with residual gas particles in the transfer beamline. This is especially critical in sources, where the ions are created in a high-pressure environment, or when even carried out of the source by a high-pressure buffer-gas pulse, as it is the case in an LVAP source (see section 2.2.1). It is therefore crucial to extract the ions gradually to minimize losses and heating due to collisions. A configuration of a stepwise extraction by multiple electrodes achieves this goal.

In the present setup, the sources are placed on a potential of 5 keV and the ions are accelerated through the extraction configuration to ground potential. To make the setup as flexible as possible, just the sources shall be exchanged, keeping the extraction system as well as the transfer beamline untouched. Therefore, the extraction system has to be applicable to a large variety of primary beams.

Here, an ion beam with parameters as expected to originate from a LVAP source is used to simulate the extraction configuration. To minimize the pressure behind the source, this configuration includes a skimmer of 1 mm orifice (see figure 3.1) to efficiently separate most of the buffer-gas from the ions. This not only acts as a differential pumping unit, but also considerably reduces the ions' distribution in the phase space, resulting in a very narrow beam already entering the extraction setup. Furthermore, the skimmer itself influences the field induced by the first electrode (as will be shown in section 3.2.3) and therefore influences the shape of the beam.
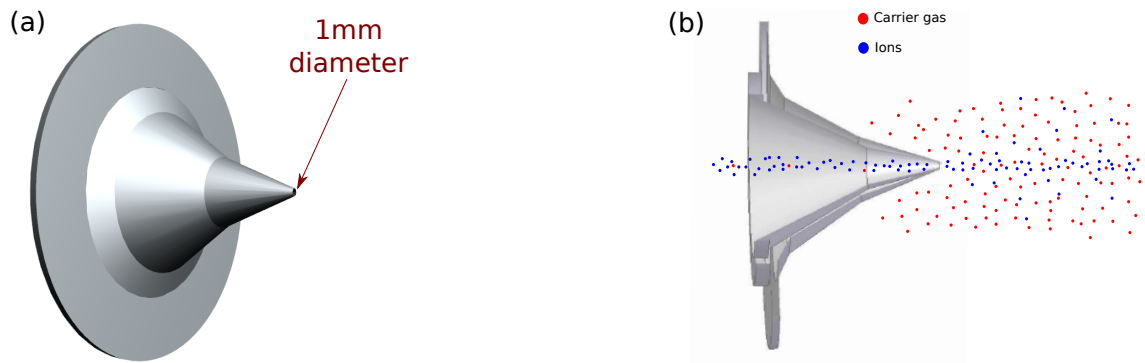

Figure 3.1: Skimmer used in the LVAP source: (a) Outer structure, (b) Inner structure. The red/blue dots represent the carrier gas/ions of interest, respectively.

The principle extraction setup is displayed in figure 3.2. It consists of multiple identical, cone-shaped electrodes, aligned along their symmetry axis. To optimize the shape of the beam, four parameters of the configuration were varied, the number of electrodes n, their opening angle α, their diameter d and the applied voltages U_1 through U_{n-1} (see table 3.1).

To limit the remaining buffer-gas flow further, a small diameter d (see figure 3.2) of the electrodes is crucial. However, in case of a small d a part of a wide beam is considerably reduced at the opening of the first extraction electrode, decreasing the ion yield. While the skimmer included in the LVAP source already causes a very small beam diameter, other sources such as the MISS produce wide beams. The setup has to find a balance between these competing factors.

To guarantee a smooth acceleration of the ions, the extraction electrodes are stacked into each other, as shown in figure 3.2, shielding the beam from the wall potential, which is 5 keV in this case. This limits the opening angle of the electrodes, which are separated by 5 mm to reduce the risk of discharges. To fulfil these conditions, the configuration has to expand along the symmetry axis with decreasing angle. The maximum available space for the extraction setup is 110 mm. The number of electrodes n is limited by this restriction as well. For large angles, however, the configuration has to expand in radial direction to guarantee the shielding from the 5 keV potential. The dimensions of the vacuum chamber, e.g. $d = 70$ mm, therefore limit the maximum opening angle.

However, more steps in the acceleration potential lead to a smoother extraction increasing the ion yield for complex molecules and clusters by decreasing the risk of
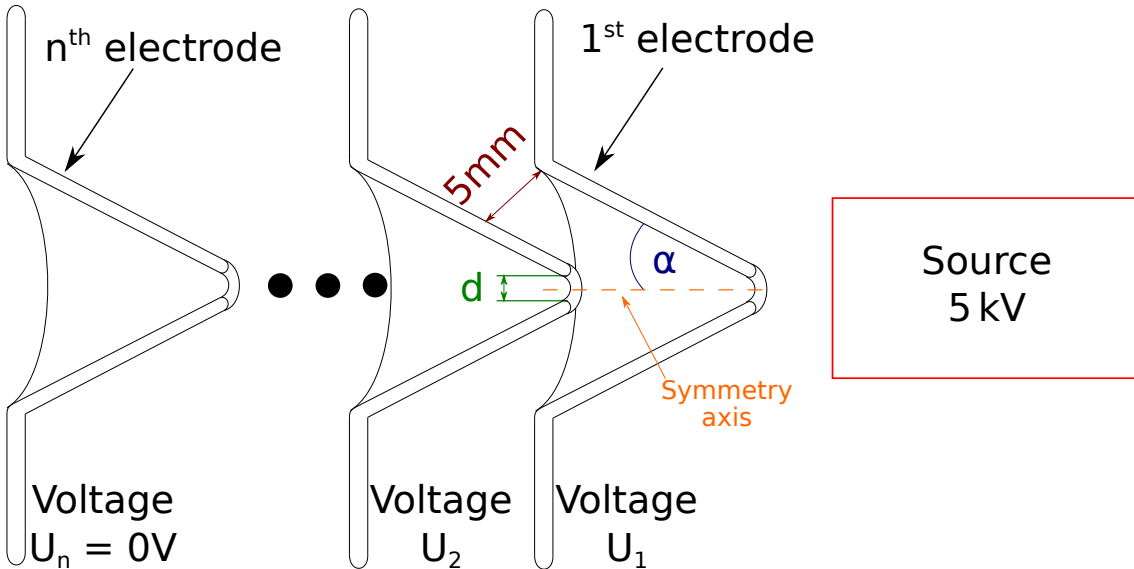

Figure 3.2: Extraction setup consistent of n electrodes with voltages U_n, diameter d, and opening angle α.

Table 3.1: Parameters, which were varied for the simulation studies.

Parameter	Range
# Electrodes n	$(1-6)$
Orifice diameter d	$(1-4)\,\mathrm{mm}$
Opening angle α	$(12-32)°$
Voltages U_n	$(0-5000)\,\mathrm{V}$

residual gas collisions. In addition, the setup is more adaptable to compensate vary-ing initial beam parameters. The voltages have to be in decreasing order ($U_i > U_{i+1}$ for $i < n$), with the last electrode on ground potential, i.e. $0\,\mathrm{V}$, to guarantee a smooth transition into the beam line, which is on ground potential as well.

3.2.2 Simulation Procedure

To find a suitable setup, different extraction configurations in combination with an LVAP source including a skimmer were simulated first. After optimizing, the skimmer was removed to analyse the setups' adaptability to sources with beams of larger emittance.

For the initial beam conditions, an ensemble of $1,000$ ions with a cone shaped velocity distribution with an opening angle of $1°$ and a Gaussian distribution in the position with $\sigma = 0.5\,\mathrm{mm}$ were used. No energy distribution was assumed. The configuration was optimized on the extracted beam shape alone. First test simulations with varying initial beam parameters had shown, that wider beams
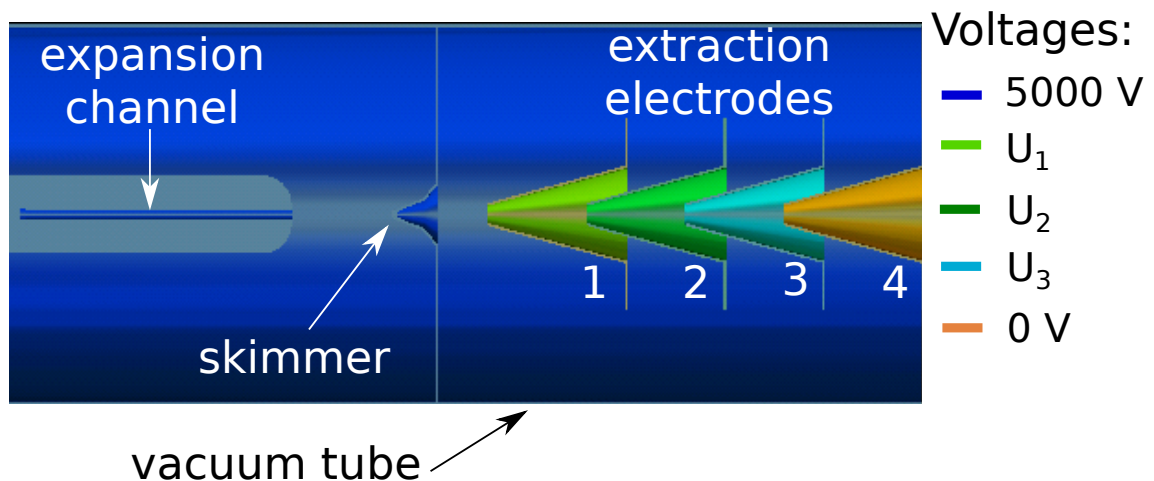

Figure 3.3: Extraction configuration implemented in SIMION. Voltages are assigned according to the colour code.

only resulted in a smaller efficiency, but had no impact on the shape of the extracted beam. Therefore, the initial distribution was chosen such that all ions would pass the setup.

The realization of an exemplary configuration in SIMION is displayed in figure 3.3. Here, four electrodes with an opening angle of $\alpha = 15°$ and an orifice diameter $d = 4\,\mathrm{mm}$ are placed behind the skimmer. They are centered in a tube to simulate the vacuum chamber.

The design goal of the configuration is the extraction of a narrow (beam diameter $d_b < 5\,\mathrm{mm}$), parallel ion beam. As a reference point, at which the shape of the beam is optimized, serves the entrance of an electrostatic cylindrical deflector, the first element of the 5 keV transfer beamline, following 676 mm behind the skimmer. The size of the extracted beam, here presented by the average distance of the particles from the center of the beam, is calculated and compared for different opening angles, orifice diameters, applied voltages and number of extraction electrodes (see table 3.1). While the ion optics partly act as focusing elements on the beam, the reference point is in a field free region where particles fly ballistically.

3.2.3 Simulation Results

The first simulations were done using four extraction electrodes. As an initial step, the voltages and angles were varied for configurations with 3 mm (figure 3.4 (a)) and 4 mm orifice diameter (figure 3.4 (b)).

While many potential configurations produce beam diameters nearly independent of the opening angle, the ones using exponential acceleration of the ions yield a clear minimum. The voltage schemes can be roughly divided into three groups, going by the effect they have on the beam.

The first set of potentials are nearly constant with the opening angle and cause a relatively broad beam. Representatives of this group are the configurations 3.4(2) and 3.4(8). Both have first a relatively small potential difference to the source
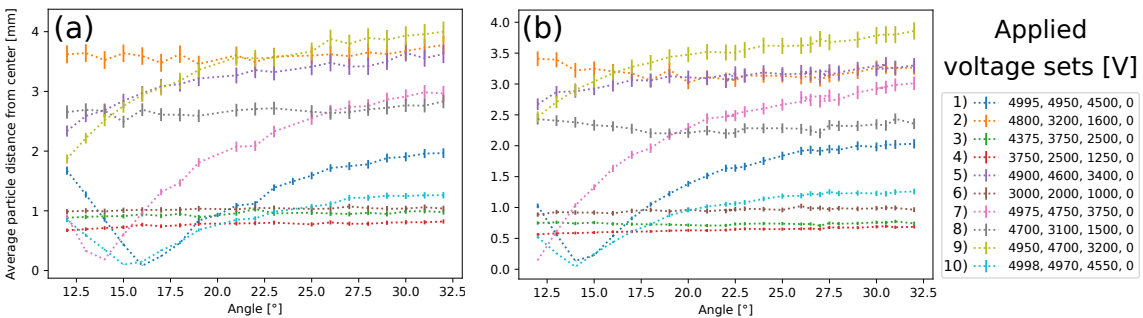

Figure 3.4: Beam diameter for varying voltages of a configuration of four extraction electrodes with 3 mm diameter (a) and with 4 mm diameter (b)

($U_{source} = 5000\,\mathrm{V}$) and then use (nearly) equidistant steps to reach ground potential. This group will further be referred to as group (I).

The second group, (II), consist of voltage sets 3.4(3), 3.4(4) and 3.4(6). The sets 3.4(4) and 3.4(6) use equidistant steps, while the potential difference for 3.4(3) increases between each two electrodes by a factor of two.

The third group, (III), displays a strong dependence of the beam diameter on the opening angle. While the voltage sets behave similar to group (I) for large angles, the particles' average distance from the center drops well below even group (II) at about 15°. Whereas this effect is only just visible for sets 3.4(5) and 3.4(9) in the considered region of angles, 3.4(1), 3.4(7) and 3.4(10) display a clear minimum at 14°, 15° and 16° for the $d = 3\,\mathrm{mm}$ setups, respectively. Here, the potentials differences increase exponentially.

Furthermore, a shift of the beam diameter minimum towards smaller angles is visible for increasing extraction electrode diameters. The optimal angles for the voltage sets 3.4(5), 3.4(9) and 3.4(10) using a configuration with $4\,\mathrm{mm}$ orifice diameter are 12°, 14° and 15.5°, respectively. The angle independent configurations display little dependence on d. To increase the ion yield, an electrode diameter of
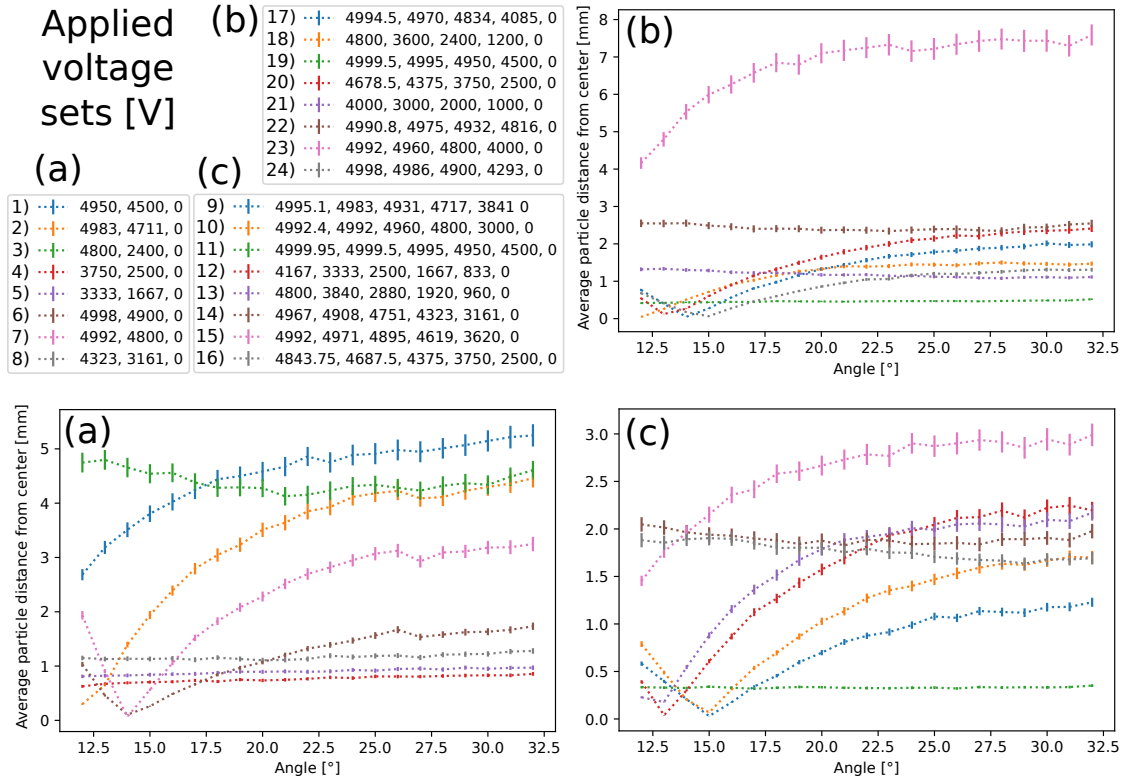

Figure 3.5: Extracted ion beam size for various voltage sets with $4\,\mathrm{mm}$ orifice diameter. The number of electrodes is 3 (a), 5 (b), and 6 (c).

4 mm is used in the following.

In a next step, voltage sets for configurations of three (see figure 3.5 (a)), five see (figure 3.5 (b)) and six (see figure 3.5 (c)) extraction electrodes were studied for various opening angles. Again, sets from all three potential groups were used. They display similar behaviour as for four electrodes shown in figure 3.4. Low and high
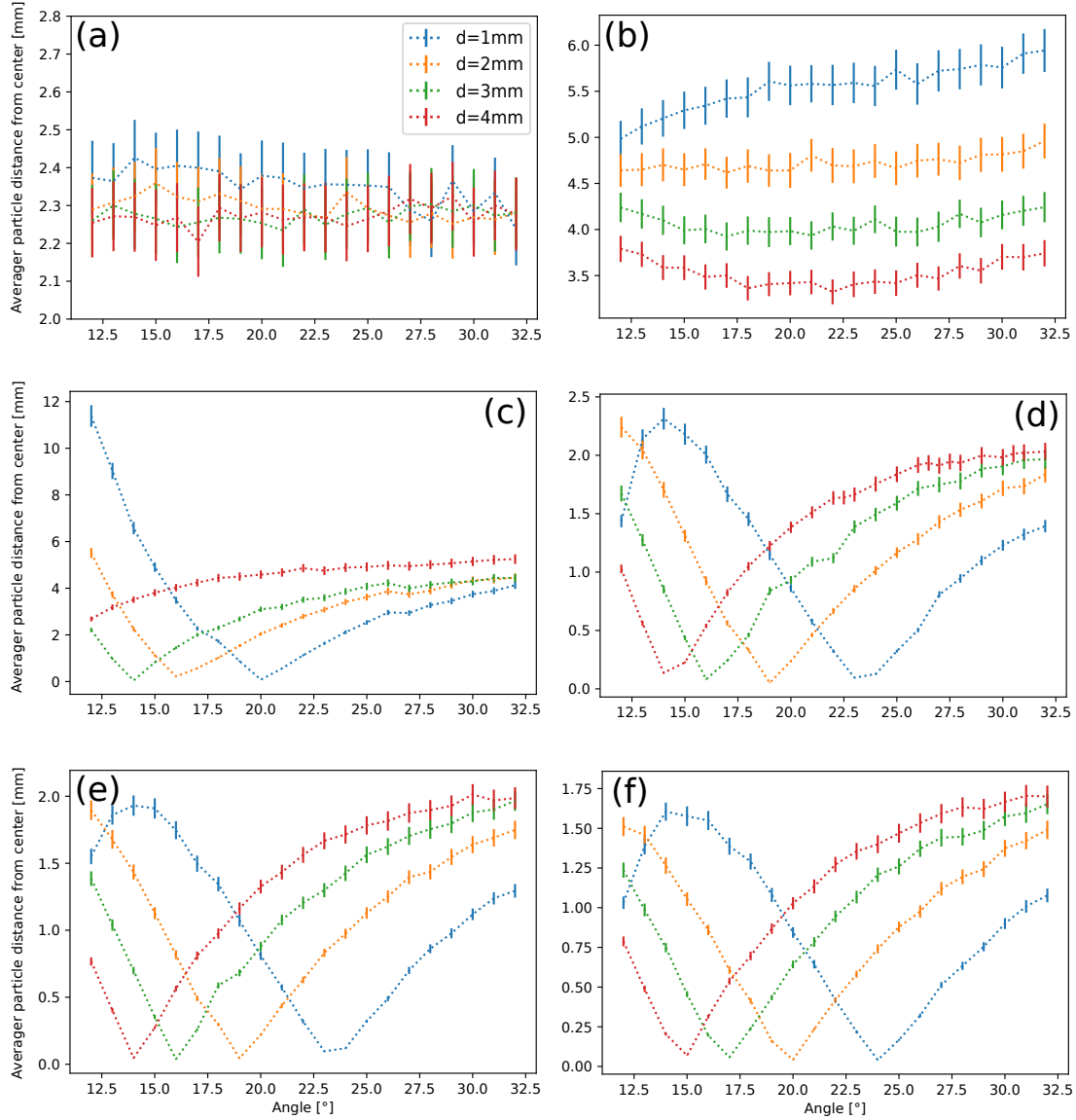

Figure 3.6: Beam diameter for varying electrode diameters and various number of electrodes. (a) 1 electrode, (b) 2 electrodes, (c) 3 electrodes, (d) 4 electrodes, (e) 5 electrodes, (f) 6 electrodes. Applied voltages are listed in table 3.2.

Table 3.2: Applied voltages for figure 3.6, with $n = 1, 2, .., 6$ electrodes

# Electrodes	Applied voltages (V)
1 (a)	$U_1 = 0\,\text{V}$
2 (b)	$U_1 = 4500\,\text{V}$, $U_2 = 0\,\text{V}$
3 (c)	$U_1 = 4950\,\text{V}$, $U_2 = 4500\,\text{V}$, $U_3 = 0\,\text{V}$
4 (d)	$U_1 = 4995\,\text{V}$, $U_2 = 4950\,\text{V}$, $U_3 = 4500\,\text{V}$, $U_4 = 0\,\text{V}$
5 (e)	$U_1 = 4994.5\,\text{V}$, $U_2 = 4970\,\text{V}$, $U_3 = 4834\,\text{V}$, $U_4 = 4085\,\text{V}$, $U_5 = 0\,\text{V}$
6 (f)	$U_1 = 4995.1\,\text{V}$, $U_2 = 4983\,\text{V}$, $U_3 = 4931\,\text{V}$, $U_4 = 4717\,\text{V}$, $U_5 = 3841\,\text{V}$, $U_6 = 0\,\text{V}$

average particle distances to the center nearly independent of the opening angle of the extraction electrodes were observed as well as configurations with clear minima.

Voltage sets from group (III) were then taken for each $n = 3, 4, 5, 6$ electrodes configuration and the impact of varying electrode diameters was studied (see figure 3.6). For comparison, setups consistent of one or two electrodes were also simulated. The applied voltages are listed in table 3.2.

For $n \geq 3$, the minimum of the particles' average distance to the center of the beam shifts towards smaller angles for increasing electrode diameters (see figure 3.6). Furthermore, this effect seems to decrease with increasing d. For $n = 1, 2$, the beam size appears to stay relatively constant.

From figures 3.4 - 3.6 it is obvious, that low beam divergence can be achieved by choosing proper opening angles and voltages, independently of the number of electrodes, for $n \geq 3$. To find a compromise between the length and the adaptability of the setup (see section 3.2.1), a configuration of four electrodes was chosen as the best option.

To guarantee a high ion yield for sources with wider initial beams (e.g. MISS), the diameter of the electrodes was furthermore set to 4 mm. This should not increase the pressure behind the extraction significantly for the LVAP source, since the skimmer orifice of 1 mm already keeps out most of the carrier gas and the remaining residual gas particles still have to make it through four narrow openings to pass the extraction. The shape of the electrodes themself also favours the removal of ballistically flying neutral particles.

Last, the effect of the skimmer on the diameter of the extracted beam was analysed. With the now specified configuration of four extraction electrodes with 4 mm diameter, a setup without a skimmer was then used to study the effects of varying voltages and opening angles on the ions average distance from the beam center again (figure 3.7).

Three potential sets (figure 3.7 (a)) were used, one from each of the three groups

discussed in figure 3.4. While voltage set 3.4(2) causes a relatively high beam divergence nearly independent of the opening angle for the setup including a skimmer, set 3.4(3) also displays little dependence on α but lower average particle distance from the beam center in figure 3.4 (b). Set 3.4(1) has a strong dependence on the opening angle of the electrodes for configurations including skimmers.

All three voltage sets show a dependence on the opening angle (figure 3.7 (a)), however none as significantly as the configurations that include a skimmer. Furthermore, set 3.7(1) produces the lowest average particle distance to the beam center. That was therefore used for configurations with varying skimmer diameters d_s (figure 3.7 (b)).

Here, the shape of the curves is independent of the skimmer diameter and only changes significantly, when no skimmer is implemented. The curves, however, are lower at larger opening angles for smaller d_s. In the absence of a skimmer, the beam divergence behaves very differently in dependence of the opening angle. An explanation for this is indicated by the equipotential lines induced by the different configurations, as shown in figure 3.8.

The skimmer is at the same potential as the source (figure 3.3). Therefore, the outreach of the extraction potential is greatly influenced by the skimmer. While the electrodes have a focusing effect on the beam in both configurations, the reshaping of the field lines by the skimmer can cause a focus point in front of the first electrode as well.

Figure 3.8 shows the field lines (red) for configurations with (a) and without skimmer (b) and four extraction electrodes with an orifice diameter of 4 mm and an opening angle of 15°. A focus point before the first extraction electrode can be observed in figure 3.8 (a), but not in (b).
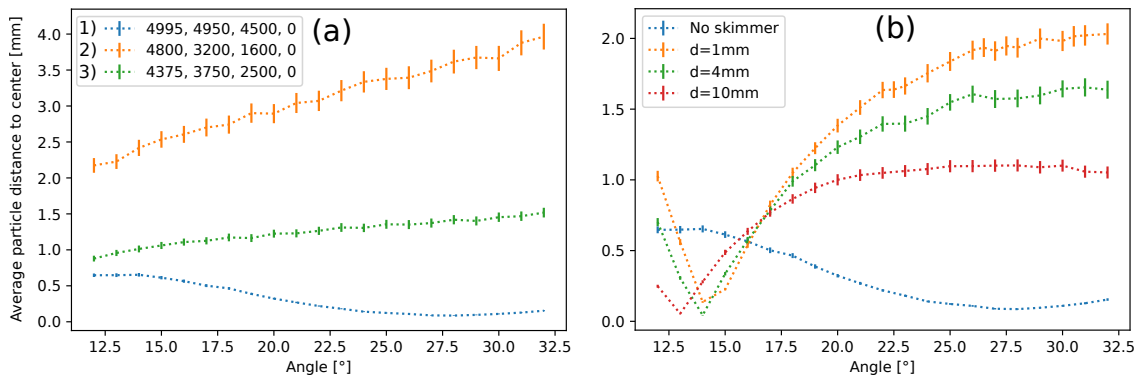

Figure 3.7: (a) Varying voltages for a configuration with four extraction electrodes of 4 mm diameter without skimmer, (b) Varying skimmer diameter for a configuration with four extraction electrodes of 4 mm diameter and voltages ($U_1 = 4995$ V, $U_2 = 4950$ V, $U_3 = 4500$ V, $U_4 = 0$ V).

With these informations, a suitable extraction configuration can be further specified. Next to $n = 4$ and $d = 4$ V, figure 3.7 (b) shows, that the opening angle has a far greater impact on the diameter of the extracted beam for setups including skimmers. From figure 3.4 (b) it is further known, that minima in the average particle distance from the center seem to occur for small angles. Choosing $\alpha = 15°$ therefore is a good compromise between configurations with and without skimmer. An exponentially decreasing voltage set with a minimum at this setup with skimmer (figure 3.4 (b)) could be found, set 3.4(1), and even without a skimmer, the average particle distance from the center is still in a reasonable range (figure 3.7 (b)).

Therefore, the extraction setup has been designed with the following parameters: number of electrodes $n = 4$, their orifice diameter $d = 4$ mm, and their opening angle $\alpha = 15°$.
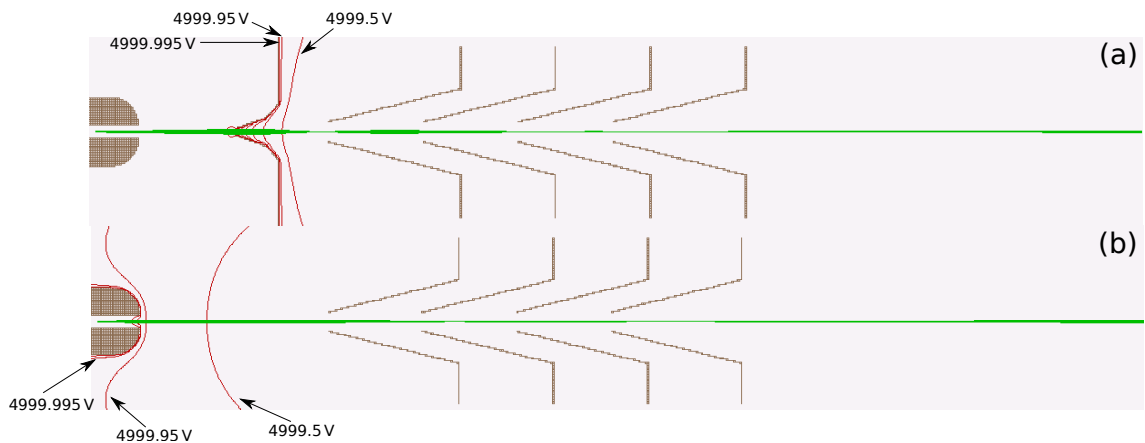
Figure 3.8: Field lines for a extraction configuration consisting of four electrodes with an orifice diameter $d = 4$ mm and an opening angle $\alpha = 15°$ including a skimmer (a) and without a skimmer (b)

4 Analysing the molecular composition of a stored ion beam

This chapter focuses on the mass separation prior injection into CSR and the identification of the molecular composition of the stored ion beam. This is done in three steps. First, the bending magnets 1 and 2 (see figure 4.1) are employed for mass selection (section 4.1). To verify the mass in a second step, the revolution time of a short ion bunch injected into CSR is then determined (section 4.2). To this end, two methods were developed and discussed. In the first, the bunch itself is observed by neutral events, which either occur due to electron autodetachment and autofragmentation or by collisions with residual gas particles, or being induced by overlapping the light of a continuous wave laser. In the second one, a laser-excited subset of the bunch is monitored by delayed electron emission. Third, to identify the isobaric composition, a fragment scan is performed (section 4.3). The ion beams of Co_4^- (mass 236 u) and C_4O^- (mass 64 u) are analyzed and discussed (section 4.4).
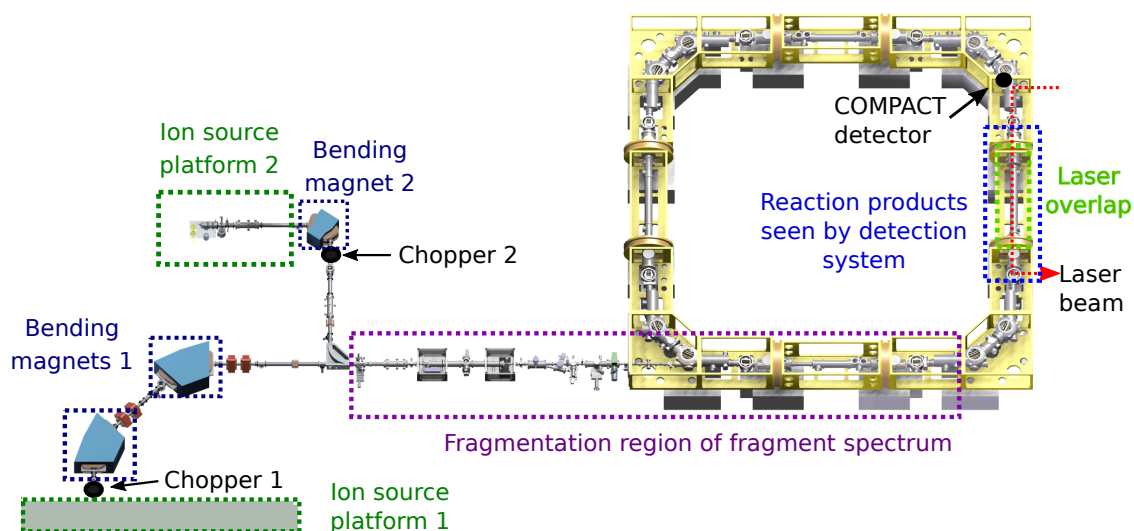
Figure 4.1: Schematic drawing of the CSR and its injection beam lines. For details see text.

4.1 Mass seperation by bending magnets

The bending magnets in the transport beam lines between the ion source platforms and the CSR (see figure 4.1) are used as mass separators. For a fixed kinetic energy, a range Δm of masses which can pass the magnets is given by

$$\frac{\Delta r}{r} = \sqrt{\frac{\Delta m}{m}}, \tag{4.1}$$

using eq. (2.3). Here,r is the bending radius and Δr determines the effective exit diameter, e.g. slits, behind the magnets. Δm is defined as the width of the peak at 10% of its height. A Faraday cup located closely behind the magnets is used to acquire a mass spectrum in dependence of the magnetic field. The resolving power of the magnets for an ideal beam neglecting any momentum spread is given by

$$R = \frac{m}{\Delta m} = \left(\frac{r}{\Delta r}\right)^2. \tag{4.2}$$

Thus, ions with masses higher than $R \cdot u$, u being the atomic mass unit, cannot be resolved. In reality, this value is considerably reduced by the momentum spread ($\propto R$) of the beam. Hence, the emittance of the ion beam reduces the effective resolution. Thus, a beam with low emittance, as discussed in chapter 3, is favorable. Nevertheless, a mass verification after the selection is required.

4.2 Determining the revolution time

To confirm the selected mass, a measurement of the stored ions' revolution time is performed. Although the ring is electrostatic and therefore stores all particles with a kinetic energy being in the acceptance of the CSR independently of mass (see section 2.1.1), the velocity of the ions, and therefore their revolution time, is mass dependent:

$$v(m) = \sqrt{\frac{2E}{m}}. \tag{4.3}$$

Knowing the circumference C of the closed orbit, the revolution time t_r for an ion bunch with mass m can be calculated:

$$t_r = \frac{C}{v(m)} = C\sqrt{\frac{m}{2E}}. \tag{4.4}$$

Two methods to determine the revolution time are discussed below.

4.2.1 Observing an ion bunch by residual gas collision and spontaneous decay

Typically, ions are injected as a bunch into CSR, created by a chopper either directly after the source platform (chopper 1) or after the bending magnet (chopper 2) (see figure 4.1). Neutralized particles from residual gas collisions or the spontaneous decay of rovibrationally excited ions in the straight section in front of COMPACT are counted. Due to the bunched signature of the coasting ion beam, the obtained signal is periodical with a frequency corresponding to the revolution frequency of the beam. By choosing a chopper time sufficiently below the expected revolution time, the bunches can be resolved (see inset figure 4.2).

The precision of this measurement is limited by the broadening of the ion bunch, due to its momentum spread and ion-ion interactions. It reaches its maximum resolution just before the ion bunch spreads out over the entire closed orbit of the storage ring. For an isobaric beam in the CSR, this debunching can be observed after a few hundred revolutions. Simulations of the debunching effect are shown in figure 4.3 [33]. The initial bunch width equals half of the CSR circumference. Although a weak peak structure can still be observed after more than 1500 revolutions, the gap of the ion beam in the ring closes at about 200 revolutions. The simulation takes two variables of the beam into account. One is the momentum spread of the ions $(\frac{\Delta p}{p})$, which describes the momentum distribution within the beam. The other is the slip factor

$$\eta = \frac{\Delta f/f}{\Delta p/p},\tag{4.5}$$

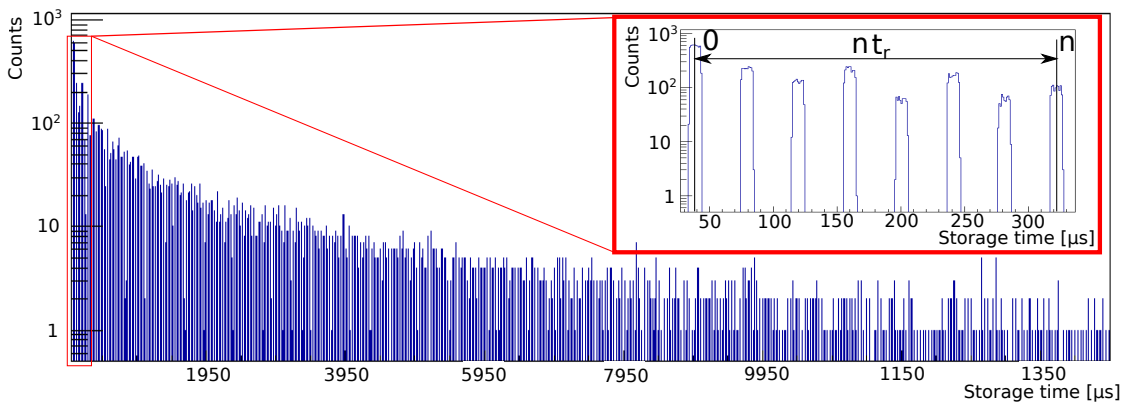with the revolution frequency f and the frequency deviation of the ions from the

Figure 4.2: Neutralization signal in dependence of storage time; Inset: Zoom of the first 350 µs, showing the bunched signature of the signal

center particle Δf. For beams in the CSR, they are $\frac{\sigma_p}{p_0} = 10^{-3}$ and $\eta = 0.686$, respectively, which were estimated previously [34].

For an ion beam containing multiple masses due to insufficient mass separation of the bending magnets, the difference in the revolution frequency causes a faster dispersion of the bunches. With a chopper time of

$$t_c = x t_r(m) \tag{4.6}$$

with $x \leq 1$ and $t_r(m)$ being the revolution time of the lighter ion, the time difference between the length of the bunch and circumference of the ring, neglecting broadening due to momentum distribution and ion-ion interactions, is given by

$$\Delta t = (1 - x) t_r(m). \tag{4.7}$$
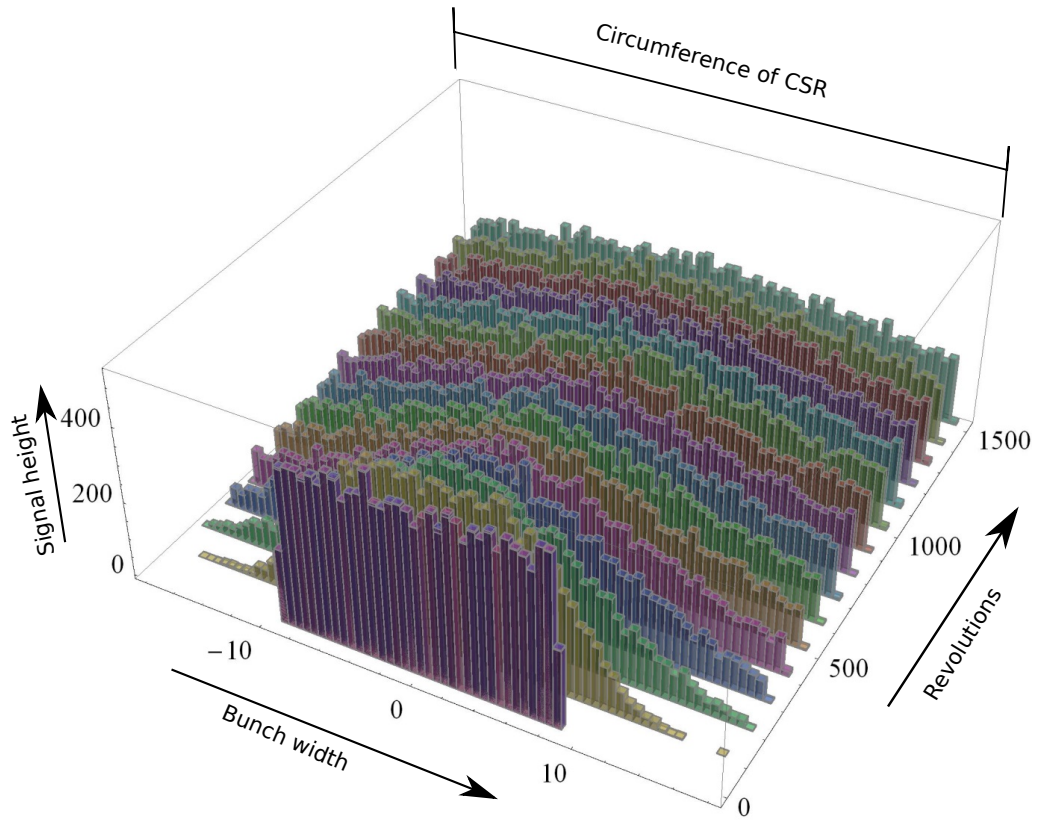
Figure 4.3: Simulations of the bunch dispersion in dependence of the number of revolutions in CSR. The initial bunch width is half the ring circumference [33].

For a contamination with ions of mass $m + \Delta m$, the heavier fraction of the beam has a longer revolution time and Δt is therefore reduced by the difference of the revolution times multiplied by the number of revolutions N:

$$\Delta t = \quad (1 - x)t_r(m) - N(t_r(m + \Delta m) - t_r(m)) \tag{4.8}$$

$$= \quad \frac{C}{\sqrt{2E}}((1 - x)\sqrt{m} - N(\sqrt{m + \Delta m} - \sqrt{m})), \tag{4.9}$$

with C being the circumference of the ring and using eq. (4.4). In the case of $0.5 \leq x < 1$ it takes

$$N = (1 - x)\frac{\sqrt{m}}{\sqrt{m + \Delta m} - \sqrt{m}} \tag{4.10}$$

revolutions for Δt to reach zero and hence for the bunches to spread over the entire closed orbit of the storage ring. If $0 < x < 0.5$, the two species are separated when $\Delta t = (1 - 2x)t_r(m)$, which is after

$$N = x\frac{\sqrt{m}}{\sqrt{m + \Delta m} - \sqrt{m}} \tag{4.11}$$

revolutions.

4.2.2 Revolution time obtained by delayed electron emission

Delayed electron emission or delayed fragmentation due to laser excitation is a statistical process in clusters and larger molecules ($N_{atoms} \geq 3$) [35]. Single photon
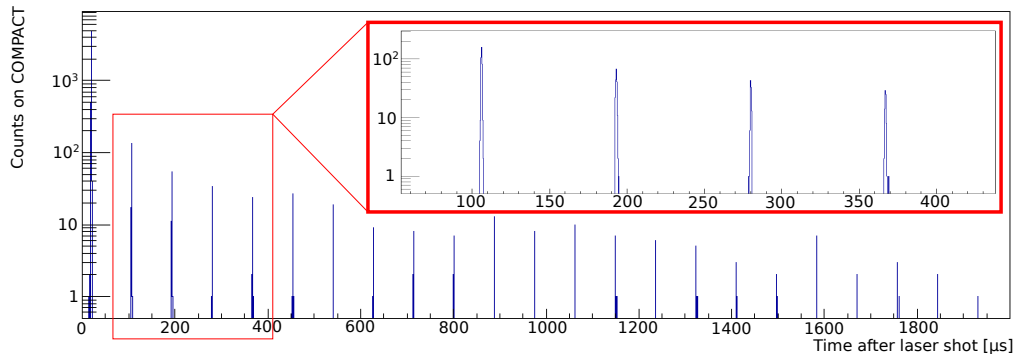
Figure 4.4: Delayed events of the Co_4^- cluster for a photon energy of 1.635 eV in dependence of time after laser excitation; Inset: Zoom into the first $450\,\mu s$ showing the shape of the delayed signals.

absorption of the molecular ion raises the internal energy above the electron affinity (EA). Internal conversion distributes the excitation energy over the vibrational modes leading to delayed electron emission or fragmentation. This process takes place on a time scales up to ms.

By overlapping a pulsed laser beam (see section 2.2.3) with the ion beam, only molecules in the overlap region corresponding to a narrow time window are excited, which may then statistically detach their electron. Although the excited ions can neutralize anywhere in the ring, only the ones detaching in the field free straight section of CSR in front of the detector (figure 4.1) can be recorded. The time resolution is more precise than the width of the ion bunches, which is determined by the chopper time, due to the small laser overlap region and a laser pulse width t_p of $(3 - 5)\,\text{ns}$.

For ions of velocity v, the fraction of the beam excited by the laser has a time spread Δt_{ex} proportional to the length of the laser overlap region l_l (figure 4.1).

$$\Delta t_{ex} = t_p + l_l(\frac{1}{c} + \frac{1}{v}) \approx \frac{l_l}{v}. \tag{4.12}$$

Figure 4.4 shows the sum of all delayed events from a single run of Co_4^- after laser excitation with a photon energy of $1.635\,\text{eV}$. The FWHM of the peaks is less than $3\,\mu\text{s}$. The distance between the peaks determines the revolution time of the excited fraction of the beam. This method is expected to be less sensitive to contaminations because the laser typically induces delayed events in only one of the molecular species stored in the ring.

4.3 Recording a fragment spectrum

In many sources, molecules are produced in highly excited states (see section 2.2.1) and may fragment spontaneously or due to residual gas collisions. These fragments have only a fraction of the kinetic energy of the parent molecule corresponding to the mass fraction, disregarding kinetic energy transfer:

$$\frac{m_f}{m_p} = \frac{E_{kin,f}}{E_{kin,p}}, \tag{4.13}$$

where m_f is the fragment and m_p is the parent mass.

Thus, fragments are lost with the parent settings of the ring. By setting the CSR to store $E_{kin,f}$ instead, fragments created in the straight section before the first 6° deflector in corner 2 (figure 4.1) are stored and can be detected at the closed orbit position, while the parent beam is lost. By scaling the deflector voltages all masses from $1\,\text{u}$ to the parent mass can be consecutively recorded. With the acquired masses

it is then possible to reconstruct the composition of the stored ion beam, as shown in figure 4.5.

4.4 Results

To study laser-induced detachment and fragmentation of C_4O^- and Co_4^-, both ion species were stored in CSR. In this section they will exemplary be analyzed applying the procedures presented in sections 4.1 - 4.3.

In section 4.4.1 a C_4O^- beam is studied. The mass spectrum obtained by the bending magnet and a fragment scan are employed to identify the composition of the beam, while the method from section 4.2.1 is applied to determine the revolution frequency. To compare and discuss the advantages and disadvantages of the two methods presented in section 4.2, a Co_4^- beam is evaluated in section 4.4.2 employing both procedures.

4.4.1 Identifying C_4O^- in the CSR

C_4O^- (mass 64 u) was produced in a MISS (see section 2.2.1) and then stored in the CSR. The process of mass selection and beam identification is presented in this section.

By employing a carbon target in a dilute oxygen atmosphere, the MISS could be optimized for C_4O^- production. To find the correct settings for passing mass
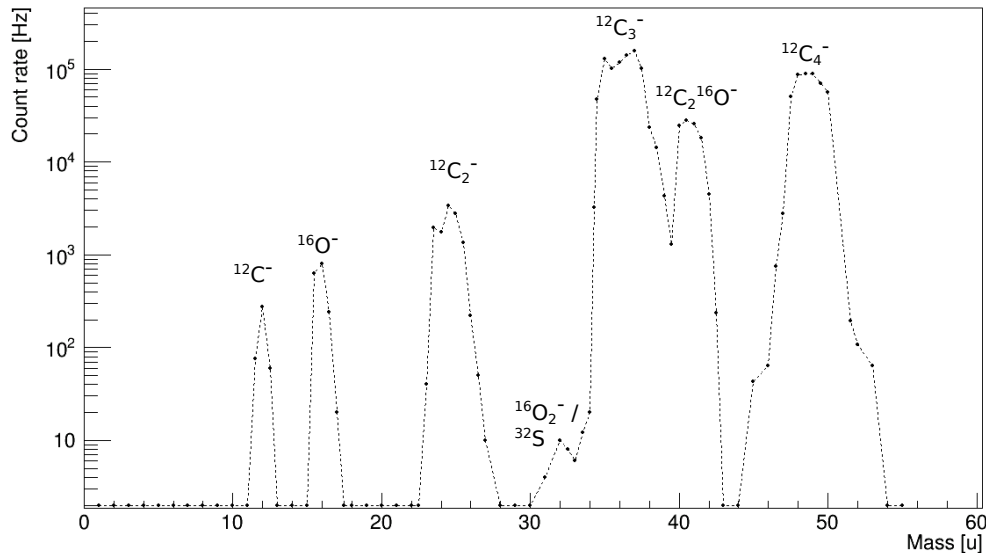
Figure 4.5: Fragment spectrum from parent ion beam of mass 64 u. MISS was set up to produce C_4O^-. For details see text.

64 u through the bending magnet, a mass spectrum was recorded at a Faraday cup behind the magnet (figure 4.1). The peaks at masses $12\,u$ (^{12}C), $13\,u$ (^{13}C), $16\,u$ (^{16}O) and $17\,u$ (^{17}O) were used for mass calibration, needed due to the hysteresis effect in the magnetic field scan.

The recorded spectra are displayed in figure 4.6. Next to the two carbon and oxygen isomers, ^{12}C and ^{13}C, as well as ^{16}O and ^{17}O, the low sensitivity scan (figure 4.6 (a)) also reveals peaks at masses 24 u, 25 u, 36 u, 48 u and 49 u, which can be attributed to pure carbon molecules C_N to the order of $N = 4$. A weak signal at 40 u is also visible and can be attributed to C_2O^-.

By increasing the current sensitivity of the cup readout, weaker beam components can be detected in a second mass scan (figure 4.6 (b)). Additional to the previous molecules, peaks at the positions of possible carbon - oxygen combinations 40 u and 41 u (C_2O^-) and $64\,u$ (C_4O^-) now appear in the spectrum. Signals at 32 u and 33 u can either be attributed to O_2^- or S^-. The later could be a contamination, because it has been produced in this source previously.
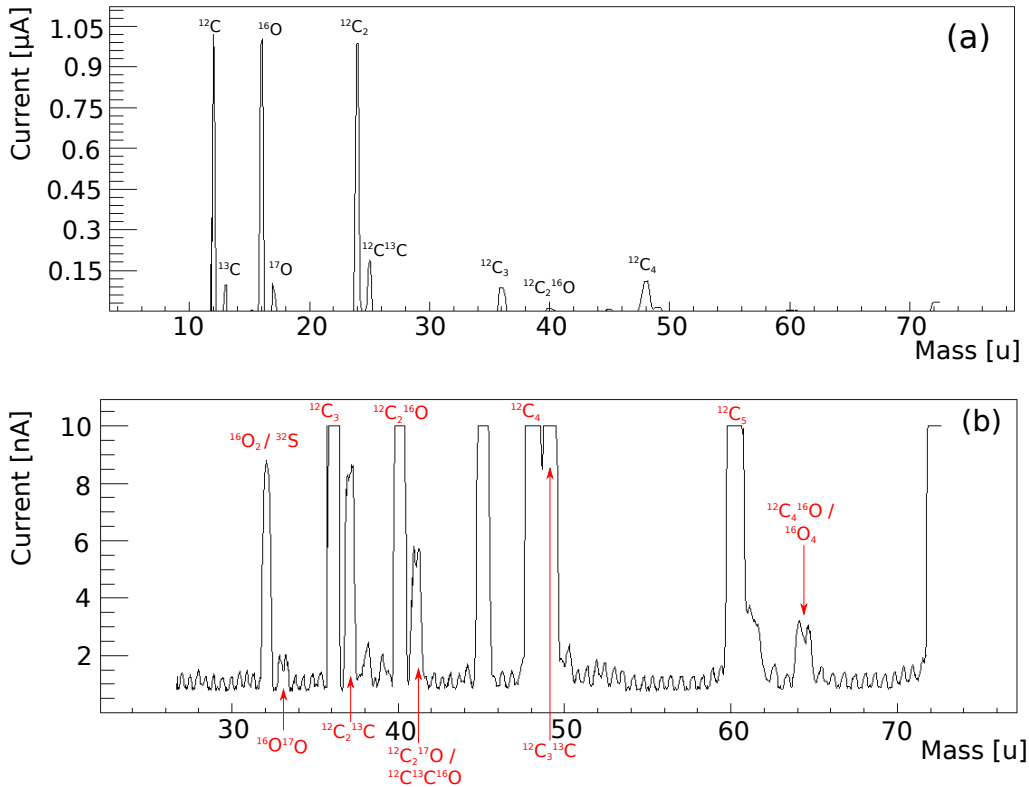
Figure 4.6: Mass spectrum from a MISS optimized for C_4O^- production. The current is measured on a Faraday cup behind the bending magnet: In (a) the saturation limit of the readout is $3\,\mu A$, while it is reduced to $10\,nA$ in (b) to increase the sensitivity.

For the peak at 45 u, only unlikely candidates could be found. The stable atomic scandium should not be present in the source and possible molecular compositions, made up of particles already identified, would need to include one heavier isotope. For example CO_2^- including either a ^{13}C or one ^{17}O. This is unlikely to be the cause of the signal due to the missing peak at mass 44 u. Since the natural abundance of the lighter isotopes are greater (see figure 4.6), a mass peak at 45 u should be accompanied with a much larger intensity of 44 u ions. Another possibility would be a double charged ($q = 2\,e$) ion. These are difficult to produce in a MISS, and can therefore also be excluded.

The peak broadening for higher masses as expected from eq. (4.1), can already be observed in figure 4.6. While the peak at mass 12 u has a width of 0.34 u at 10 % of the maximum height, for mass 32 u it is already 0.55 u. The signal-to-noise ratio of the peak at mass 64 u is very low and leads to a width of 1.2 u at 10 % of the peak height. As a consequence, a pure beam of 64 u (e.g. C_4O^-) can not be guaranteed with this resolution and has to be verified in the CSR.
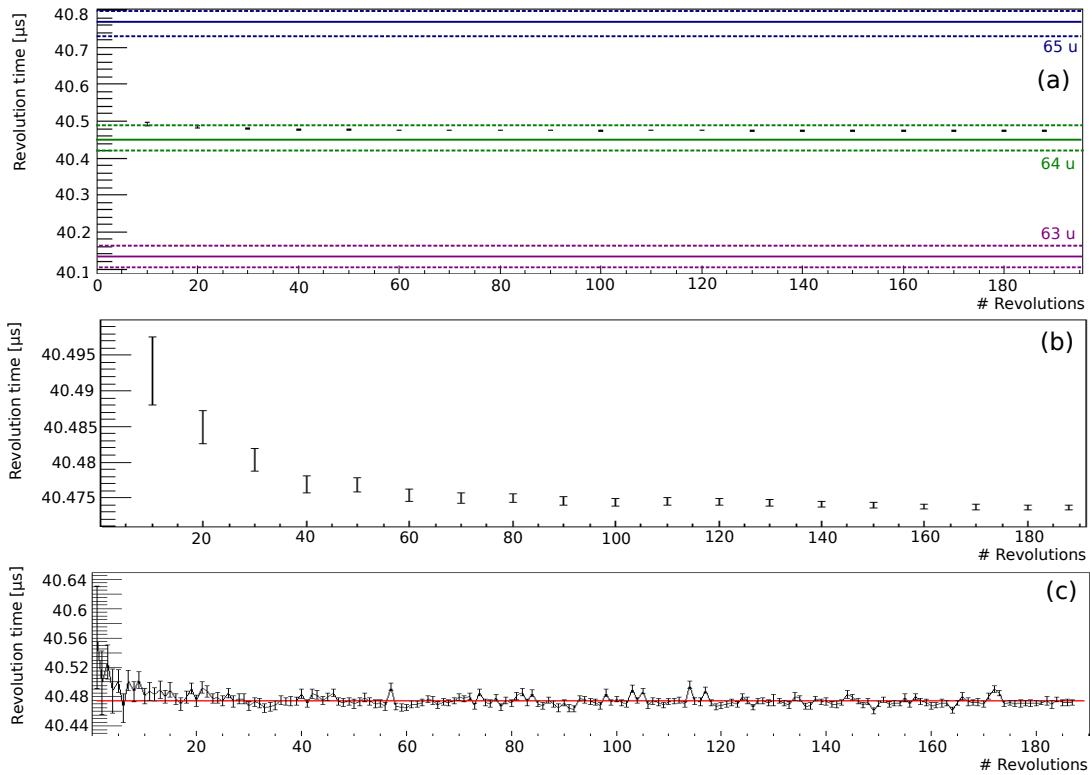
Figure 4.7: Measured revolution time. (a): Average revolution time with uncertainty dependend on the number of revolutions used for fit, (b): Zoom into (a), (c): Revolution time derived from time seperation between the first and the nth bunch signal. The red line marks the average revolution time.

The magnet was then set to select the peak at mass $64\,\mathrm{u}$ shown in figure 4.6 (b). To check this setting, the revolution time of the ions was measured using the method introduced in section 4.2.1. To chose an appropriate chopper time, the theoretical value for t_r was calculated. The circumference of the closed orbit is $C = (35.121 \pm 0.030)\,\mathrm{m}$. The uncertainty is due to the momentum spread and the betatron oscillation of the ion beam [33]. For mass $64\,\mathrm{u}$ ($\mathrm{C_4O^-}$) and a kinetic energy of $(250{,}000 \pm 10)\,\mathrm{eV}$, eq. (4.4) predicts a revolution time of $(40.452 \pm 0.035)\,\mathrm{\mu s}$. The chopper was therefore set to a bunch width of $20\,\mathrm{\mu s}$, to find a compromise between optimal resolution, which requires small bunches and the measurement time, dependent on statistic and hence on the number of ions in the ring. In comparison, mass $63\,\mathrm{u}$ and $65\,\mathrm{u}$ have revolution times of $(40.135 \pm 0.034)\,\mathrm{\mu s}$ and $(40.767 \pm 0.035)\,\mathrm{\mu s}$, respectively.

To extract t_r from the data, an algorithm was implemented, which fitted a flat top function with linear flanks over each bunch (see figure 4.2) to calculate its mean. For the statistical uncertainty of this value the method explained in [36] was applied. The time separation between the first and the n-th bunch signal was derived and divided by the number of revolutions taken. This process terminates, when the latest value for t_r differs significantly from the second last, which can either be caused by a "missing" bunch due to insufficient statistics or because debunching ultimately dissolves the bunched structure of the beam.

For the present $\mathrm{C_4O^-}$ measurement, a run with 396 injections and $\sim 20{,}000$ counts in the time window used for the fit was investigated. The algorithm terminated after 188 revolutions due to insufficient statistics, caused by the first gap in the data at $\sim 7.608\,\mathrm{ms}$. With a fit shown in figure 4.7 (c), the revolution time could be determined to be $t_r = (40.47368 \pm 0.00033)\,\mathrm{\mu s}$. The error is purely statistical. According to eq. (4.4), this corresponds to an ion mass of $m = (64.07 \pm 0.11)\,\mathrm{u}$. Thus, mass $64\,u$ is stored. The mass uncertainty decreased by a factor of ~ 11 from $1.2\,\mathrm{u}$ to $0.11\,\mathrm{u}$ compared to the resolving power of the mass spectrum shown in figure 4.6.

To estimate the number of revolutions required to determine the mass of the stored species with sufficient confidence, figure 4.7 (a) shows the derived t_r in dependence of the number of revolutions taken into account. With only 10 revolutions, $64\,\mathrm{u}$ can already be determined as the mass of the ions with 8σ significance. However, the differences in revolution time between two neighbouring masses decrease with increasing mass. Therefore, more revolutions will be necessary for heavier particles.

To analyze the composition of the beam, a fragment spectrum was recorded according to section 4.3, which is displayed in figure 4.5. Together with the spectrum acquired behind the bending magnet (figure 4.6), the composition of the ion beam can now be reconstructed.

Knowing the mass of the ions as $m = (64.07 \pm 0.11)\,\mathrm{u}$ and the charge as $q = -1\,e$, possible molecular and atomic species are listed in table 4.1, using the *National Institute for Standards and Technology* database [37]. They are analyzed according

Table 4.1: Anions with mass $m = (64.07 \pm 0.11)\,$u, taken from [37]

Anion	Mass [u]	Comment	Conclusion
FNP^-	63.9794	No peak at 14 u (N)	Unlikely
O_4^-	63.9981	In source and (possible) peaks at O^-, O_2^- and O_3^-	Likely
FH_3NSi^-	64.00	No peak at 14 u (N)	Unlikely
$H_2NO_3^-$	64.00	No peak at 14 u (N)	Unlikely
$C_3N_2^-$	64.01	No peak at 14 u (N)	Unlikely
$CH_4O_3^-$	64.0412	Radical $\rightarrow$ Unstable	Unlikely
C_4O^-	64.0427	All possible fragments are observed	Very likely
Sulfur dioxide anion (O_2S^-)	64.064	(Possible) peaks at O^-, 32 u (S^-,O_2^-) and SO^-	Likely
H_2NOS^-	64.088	No peak at 14 u (N)	Unlikely
SiC_3^-	64.1181	No peak at 28 u (Si)	Unlikely

to their likeliness to be part of the beam. Out of the ten possible candidates, six can be excluded due to missing nitrogen (14 u) or silicon (28 u) peaks in the mass scan (figure 4.6) and the fragment spectrum (figure 4.5). These would be present if either of these atoms where in the source. Furthermore, $CH_4O_3^-$ can be ruled out because of its unstable nature.

Only three ions remain, most dominant of which is C_4O^- with strong signals at all possible fragmentation channels (figure 4.5). However, a small peak at the fragment mass 32 u indicates a contamination. Both of the other possible molecules (O_4^- and O_2S^-) have fragments on that mass, being able to break of O_2^- and, in the case of O_2S^-, also S^-. It is, however, not possible to distinguish between these two using the spectra from figures 4.5 and 4.6, since their other fragments have identical masses as well, 16 u for the daughter ion O^- and 48 u for O_3^- and SO^-, coming from O_4^- and O_2S^-, respectively.

During the experiments on C_4O^-, the electron detachment of the molecule for different photon energies was studied. For this purpose, the OPO laser (see section 2.2.3) was employed to excited the ions at different frequencies. The detachment rate could then be normalised to the number of photons and the numbers of ions to search for thresholds and resonances. Although the analysis of these measurements are not part of this thesis, a preliminary result for a photon energy range of $(0.8 - 1.35)\,$eV is shown in figure 4.8. It provides another indicator as to what the isobaric contamination might be.

An onset of the electron detachment threshold observed at about 1.2 eV, which can not be attributed to C_4O^-, because it has an expected threshold of at least

2 eV [38], would suggest a SO_2^- contamination with an electron affinity of $EA = (1.107 \pm 0.008)$ eV [39]. This is more likely then a contamination of O_4^- with an EA of (0.60 ± 0.22) eV [40].

4.4.2 Observing the debunching of a contaminated Co_4^- beam

Delayed electron emission of Co_4^- clusters was studied at the Cryogenic Trap for Fast ion beams (CTF), located at the Max-Planck-Institut for Nuclear Physics in Heidelberg [28]. The required laser energy for a maximum yield of delayed events was therefore already known to be about 1.6 eV. Hence, this molecule is a perfect candidate for the revolution time determination by delayed electron emission (see section 4.2.2).

First, t_r was calculated using eq. (4.4). The Co_4^- ions with mass 236 u were stored at a kinetic energy of $(200,000 \pm 10)$ eV. This corresponds to a the theoretical revolution time of the clusters of $t_r = (86.848 \pm 0.074)$ µs, also taking the uncertainty of the closed orbit into account. For comparison the masses 235 u and 237 u have revolution times of (86.664 ± 0.074) µs and (87.032 ± 0.074) µs, respectively.

Due to the geometry of the setup (see figure 2.3), the shape of the delayed peaks is not a flat top (as can be seen in figure 4.4), in contrast to the signal of the bunch itself (figure 4.2). Therefore, a Gaussian function was applied to fit the signal. The algorithm to determine t_r and its uncertainty remains the same as in section 4.4.1.

A run with 34 injections and $\sim 20,000$ delayed counts was used. The graph is displayed in figure 4.9 (a) and estimates a revolution time of $t_t = (86.8927 \pm 0.0018)$ µs. The uncertainty only takes statistical fluctuations into account. This corresponds to a mass of $m = (236.24 \pm 0.40)$u, using eq. (4.4). The excited fraction of the beam therefore has a mass of 236 u.

For comparison, the revolution time was determined by observing the injected
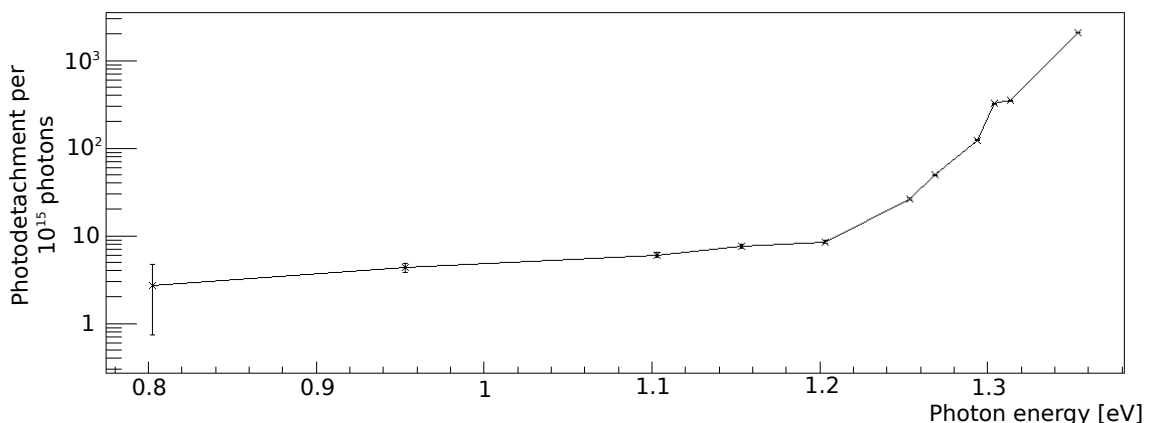
Figure 4.8: Electron detachment threshold observed in a mass 64 u ion beam

ion bunch as discussed in 4.2.2 and 4.4.1, using a run with 1000 injections and $\sim 50,000$ counts in the time window used for the evaluation. This, however, yields $t_r = (86.7261 \pm 0.0033)\,\mu s$ (figure 4.9 (b)), suggesting a mass $m = (235.34 \pm 0.40)\,u$. This is in contradiction to the measurement obtained by delayed electron events. Furthermore, a clear debunching of the signal could be observed well before the ~ 200 revolutions expected for this effect to take place due to the momentum spread of the ions (see figure 4.3).

Figures 4.10 (a) - (c) display the debunching of the Co_4^- signal, while (d) -(f) provide a comparison to an isobaric beam (C_4O^-, mass $64\,u$). While the rectangular structure is visible in both cases at the first few revolutions (a & d), a disintegration of the contaminated beam's signal is visible after 37 revolutions (b), whereas the other's remains intact (e). After 70 revolutions, the integrity of the bunch shape of the Co_4^- beam is almost completely lost (c), while the C_4O^- signal (f) shows no
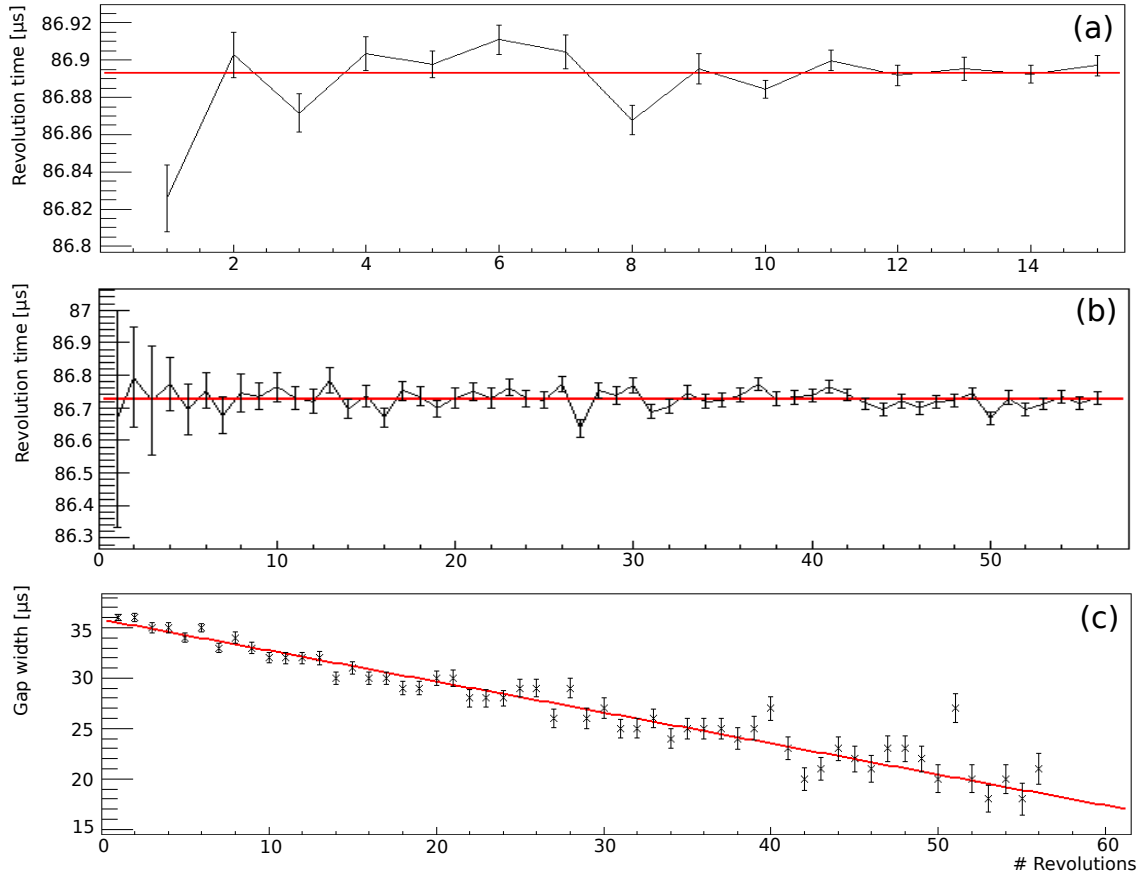
Figure 4.9: Fits to determine the revolution times: (a) Using delayed electron emission, (b) Observing the bunch in the CSR, (c) Analyzing the debunching of the beam

significant broadening compared to the first revolutions (d).

This is a clear indicator for mass contamination (see section 4.2.1). Since the debunching of the beam now happens much faster than purely caused by the momentum spread (figure 4.10), only the effects caused by mass contamination can be considered. The reduction of the gap between the revolutions Δt can then be estimated to equal the difference between the t_r of the heaviest and the lightest ion in the beam, as predicted by eq. (4.8). Figure 4.9 (c) shows the gap width Δt plotted versus the number of revolutions for the contaminated beam from figure 4.9 (b). According to eq. (4.8), the absolute value of the slope corresponds to $t_r(m + \Delta m) - t_r(m)$. Using a linear fit, the revolution time difference can be estimated to be $\Delta t_r = (0.3074 \pm 0.0069)\,\text{µs}$.

From the measurement using delayed electron emission one of the masses in the ring is already known to be $236\,u$, and the fact that the bunch observation method gave a smaller value for t_r suggests, this is the heavier part of the beam $(m + \Delta m) = 236\,\text{u}$. Using the revolution time obtained from figure 4.9 (a) ($t_t = (86.8927 \pm 0.0018)\,\text{µs}$) for mass $236\,\text{u}$, t_r for the lightest ion in the beam can than be calculated by subtracting Δt_r, to be $t_r(m) = (86.5853 \pm 0.0091)\,\text{µs}$. Employing eq. (4.4), the mass of this species therefore equals $m = (234.57 \pm 0.40)\text{u}$, considering the uncertainties of $t_r(236)$, of Δt_r, of the kinetic energy E_{kin} and the closed orbit.
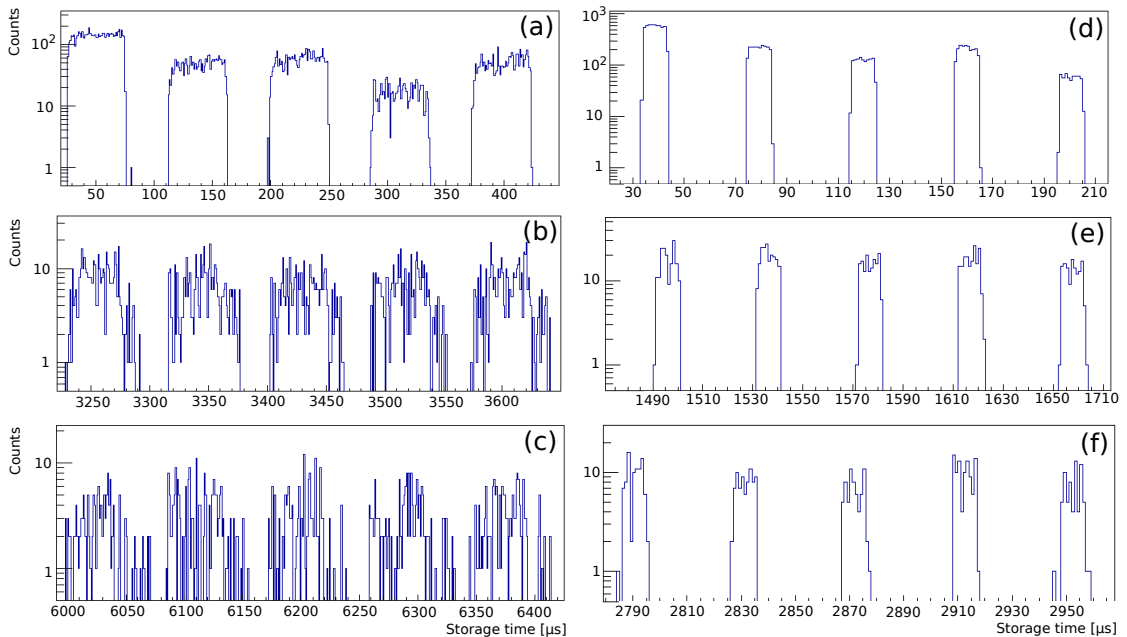
Figure 4.10: Debunching of a beam signal containing more than one mass (a-c) in comparison to an isobaric beam (d-f). (a) & (d): Revolutions 1-5, (b) & (e): Revolutions 37 -41, (c) & (f): Revolutions 69 - 73

The beam is therefore contaminated with ions of either mass 234 u or 235 u or both. This was most likely caused by insufficient mass separation by the bending magnets, which have a resolution $R = (134 \pm 5)$ for a kinetic energy of 200 keV, measured with other beams previously.

This method can only distinguish between the heaviest and the lightest ion in the beam. It can not be used to detect any masses in-between. Although the delayed electron emission was used in this example to determine one of the masses, this is not necessary to calculate the range of masses in the beam. If section 4.2.2 can not be applied, the time seperation between the beginning of the bunch signals (figure 4.2) can be used to estimate t_r for the lightest ion and the fit demonstrated in figure 4.9 (c) can then be employed to calculate the heaviest component of the beam.

However, if delayed electron emission can be induced for one of the particles, it is advantageous to use this method. The procedure requires less statistics (34 injections for figure 4.9 (a) compared to 1000 injections for figure 4.9 (b)) and can be significantly more precise for fast debunching beams, where the beginning of the signal for a revolution can not be distinguished from the next after short storage times (figure 4.10). As mentioned in section 4.2, this method is unable to detect the contamination in the beam, though. Thus for heavy beams, where a contamination due to the magnet resolution is likely, an analysis of the debunching must be done.

As the CSR continuous to store heavier beams in the coming years, the procedure demonstrated in this example to determine mass contamination will gain significance. However, if the uncertainty about the closed orbit length of the CSR can not be improved (right now at 0.85 % of the value), this method will soon reach its limits. Even for the example beam of mass 236 u and an energy 200 keV, the difference in revolution time between two neighboring masses is already 2 % of the smaller revolution time. To achieve the necessary resolution to distinguish between much higher masses, the momentum spread of the beam has to be reduced, which might be possible by cooling the bunch prior to injection with an RFQ.

5 Conclusion and Outlook

An extraction configuration consisting of four cone-shaped electrodes with an opening angle $\alpha = 15°$ and an orifice diameter $d = 4\,\mathrm{mm}$ was successfully designed for the extraction of ions from different ion sources to the transfer beamline of the CSR. The results are presented in chapter 3. It focuses on creating a low divergence beam for sources of high and low initial emittance. Furthermore, a strong dependence of the average particle distance to the beam center on the opening angle of the electrodes for specific voltage sets could be identified.

The extraction setup in combination with a standard Penning ion source scheme is currently under commission on a test bench to determine the operational settings. First results are expected in a few weeks.

An analysis tool for the composition of a stored ion beam was developed and successfully applied. The method was able to determine the revolution frequency of the ions both by observing the bunch in the ring and by inducing delayed electron emission. The sensitivity and precision of the procedures were demonstrated and the uncertainty of the closed orbit circumference inside CSR could be identified as the current resolution limit.

Furthermore, an isobaric contamination in a beam of mass $64\,\mathrm{u}$ could be detected and the various molecules could be identified using a fragment spectrum. The mass range in a beam containing multiple masses was determined by analysing the dispersion of an ion bunch in the CSR.

The exemplary beams of $\mathrm{C_4O^-}$ and $\mathrm{Co_4^-}$ showed the susceptibility of electrostatic storage devices to contaminations and demonstrated the need to check for these when storing beams of large molecules and clusters in the future.

Part I

Appendix

A Lists

A.1 List of Figures

A.2 List of Tables

B Bibliography

[1] R. von Hahn et al. *The cryogenic storage ring CSR,* Rev. Sci. Instrum. 87, 063115, 2016.

[2] W. Paul, M. Raether, *Das elektrische Massenfilter.* M. Z. Physik 140: 262, 1955.

[3] L.S. Brown and G. Gabrielse, *Precision spectroscopy of a charged particle in an imperfect Penning trap.* Phys. Rev. vol. 25, no. 4, 1982.

[4] K. Blaum, *High-accuracy mass spectrometry with stored ions.* Phys. Rep. 425, 1 − 78, 2006.

[5] S. Myers and E. Picasso, *The design, construction and commissioning of the CERN large Electron–Positron collider.* Contemp. Phys., vol. 31, no. 6, pages 287-403, 1990.

[6] D. Habs et al. *First experiments with the Heidelberg Test Storage Ring TSR.* Nucl. Instrum. Methods Phys. Res. B 43, 390-410, 1989.

[7] S. Tomita et al. *Dissociation Energy for C_2 Loss from Fullerene Cations in a Storage Ring.* Phys. Rev. Lett., vol. 87, no. 7, 2001.

[8] A.S. Schlachter et al. *Electron capture for fast highly charged ions in gas targets: An empirical scaling rule* Phys. Rev. A, vol. 27, no. 11, 1983.

[9] G. Savard et al. *A new cooling technique for heavy ions in a Penning trap.* Phys. Lett. A, 158, 247-252, 1991.

[10] H. Danared, *Electron cooling at CRYRING with an expanded electron beam.* Nucl. Instrum. Methods Phys. Res. A, 391, 24-31, 1997.

[11] R.V. Krems et al. *Possibility of buffer-gas cooling of paramagnetic carbon to ultracold temperatures.* Phys. Rev. A, 66, 030702(R), 2002.

[12] T.W. Hänsch and A.L. Schawlow, *Cooling of gases by laser radiation* Opt. Commun., vol. 13, no. 11, 1975.

[13] M. Lange et al. *Radiative cooling of Al_4^- and Al_5^- in a cryogenic environment.* New J. Phys. 14 065007, 2012.

[14] C. Meyer et al. *Radiative Rotational Lifetimes and State-Resolved Relative Detachment Cross Sections from Photodetachment Thermometry of Molecular Anions in a Cryogenic Storage Ring.* Phys. Rev. Lett. 119, 023202, 2017.

[15] D. Muell, private communications, 2018.

[16] F. Grussie, *Experimental studies of ion-neutral reactions under astrophysical conditions.* PhD, Ruperto-Carola University of Heidelberg, Germany, 2016.

[17] S. Vogel *Developments at an Electrostatic Cryogenic Storage Ring for Electron-Cooled keV Energy Ion Beams.* PhD, Ruperto-Carola University of Heidelberg, Germany, 2016.

[18] J.P. Flemming, *Penning source for ion implantation.* J. Vac. Sci. Technol. 12, 1369, 1975.

[19] R. Geller, *New high intensity ion source with very low extraction voltage.* Appl. Phys. Lett. 16, 401, 1970.

[20] R. Middleton, *A Versitale high intensity negative ion source.* Nucl. Instrum. Methods Phys. Res. 214 139-150, 1983.

[21] T.G. Dietz, M. A. Duncan, D. E. Powers, R. E. Smalley, *Laser production of supersonic metal cluster beams.* J. Chem. Phys. 74, 6511, 1981.

[22] G.M. Wells and F. Cerrina, *Differential Pumping: Is it really effective?* Nucl. Instrum. Methods Phys. Res. A, Volume 246, Issues 1–3, Pages 790-793, 1986.

[23] W. Schottky *Über spontane Stromschwankungen in verschiedenen Elektrizitätsleitern,* Annalen der Physik, 382, 23, 541–567, pages 27 and 47, 1918.

[24] K. Spruck et al. *An efficient, movable single-particle detector for use in cryogenic ultra-high vacuum environments,* Rev. Sci. Instrum. 86, 023303, 2015.

[25] A. Becker, *Imaging of Neutral Fragmentation Products from Fast Molecular Ion Beams: Paving the Way for Reaction Studies in Cryogenic Environment.* PhD, Ruperto-Carola University of Heidelberg, Germany, 2016.

[26] K. Spruck, *Dielectronic Recombination Experiments with Tungsten Ions at the Test Storage Ring and Development of a Single-Particle Detector at the Cryogenic Storage Ring.* PhD, Justus-Liebig-Universität Gießen, Germany, 2015.

[27] M. Lange et al. *Commissioning of the Heidelberg Cryogenic Trap for Fast ion beams (CTF).* Proceedings of EPAC08, 2008.

[28] C. Breitenfeldt et al. *Long-Term Monitoring of the Internal Energy Distribution of Isolated Cluster Systems,* Phys. Rev. Lett. 120, 253001, 2018.

[29] D.A. Dahl, *SIMION for the personal computer in reflection.* Int. J. Mass Spectrom. 200, 3-25, 2000.

[30] J.R. Pierce, *Rectilinear Electron Flow in Beams.* J. Appl. Phys. 11, 548, 1940

[31] J.R. Coupland et al. *A Study of the Ion Beam Intensity and Divergence Obtained from a Single Aperture Three Electrode Extraction System.* Rev. Sci. Instrum. 44, 1258, 1973.

[32] M.M. Abdelrahman and S.G. Zakhary, *Simulations Studies for Ion Beam Extraction Systems.* Braz. J. of Phys., vol. 39, no. 2, 2009.

[33] M. Griesser, private communications, 2018.

[34] M. Grieser et al. *The phase slip factor of the electrostatic cryogenic storage ring CSR* J. Phys.: Conf. Ser. 874 012049, 2017.

[35] J.U. Anderson et al. *Thermionic emission from clusters* J. Phys. B: At. Mol. Opt. Phys. 35 R1, 2002.

[36] S. Naimi et al. *Mass measurements of short-lived nuclides using the ISOLTRAP preparation Penning trap.* Hyperfine Interact 199:231–240, 2011.

[37] National Institute of Standards and Technology, https://webbook.nist.gov/chemistry/mw-ser/

[38] E. Riaplov et al. *Electronic Absorption Spectra of C_4O^- and C_4S^- in Neon Matrixes* J. Phys. Chem. A, 105, 4894-4897, 2001.

[39] M.R. Nimios and G.B. Ellison, *Photoelectron Spectroscopy of $SO_2{}^-$, $S_3{}^-$, and S_2O^-.* J. Phys. Chem. 90, 2574-2580, 1986.

[40] D. C. Conway, and L. E. Nesbitt, *Stability of O_4^-.* J. Chem. Phys. Physics, 48, 509, 1968.

Acknowledgements

I would like to thank *Manfred König* and *Maximilian Trebis*, who invested a lot of time and effort into the sources to make sure we always had a beam.

No words could ever express how thankful I am for the constant and unconditional support of my family, my parents, *Katharina Wegner* and *Helmut Schmidt*, who I owe everything to, and my sister *Laura Schmidt*.

I would also like to thank my friends for always being there for me and not being mad at me for neglecting them during the final stages of this thesis.

Erklärung

Ich versichere, dass ich diese Arbeit selbstständig verfasst und keine anderen als die angegebenen Quellen und Hilfsmittel benutzt habe.

Heidelberg, den 25.07.2018,